POLITECNICO DI TORINO

Master of Science in Bionanotechnologies Engineering

Thesis research carried out at the UNIVERSITY OF ALBERTA



Master's Thesis

Enamel Characterization and Saliva-Based Computational Modeling for Dental Caries Research

Supervisors

Prof. Jacek Adam Tuszynski
Supervisor

Prof. Svetlana Komarova
Co-Supervisor

Candidate

Alessia Santostefano
s332106

Academic Year 2025–2026

To curiosity,
the one that pushes you to look a little further,
to explore the world and not be afraid to try.

Table of Contents

Abstract 3

1 Introduction 5
1.1 Tooth and dental enamel: structure and composition 5
1.1.1 Tooth anatomy and organization 5
1.1.2 Dental enamel: formation, structure and organization 6
1.1.3 Chemical and mineral composition of dental enamel 7
1.1.4 Hydroxyapatite: structure and role in dental enamel 8
1.1.5 Human and bovine enamel 9
1.2 Dental caries and enamel mineral dynamics 11
1.2.1 Definition and clinical relevance 11
1.2.2 Enamel demineralization and remineralization 12
1.2.3 Role of pH in enamel mineral balance 13
1.3 Saliva and enamel mineral homeostasis 14
1.3.1 Human saliva: composition, functions and buffering capacity 14
1.3.2 Salivary ions and enamel mineral equilibrium 15
1.3.3 Hydroxyapatite saturation and dissolution equilibrium 15
1.3.4 Simplified saliva-like models of the oral environment 16
1.4 Shared physicochemical principles of hydroxyapatite equilibrium in biological fluids 17
1.5 Rationale and objectives of the study 18
1.5.1 Scientific gap 18
1.5.2 Specific objectives 19

2 Materials and Methods 20
2.1 Experimental methodology 20
2.1.1 Bovine enamel specimens 20
2.1.2 Sample preparation: cutting, embedding, grinding and polishing . . 20
2.1.3 Experimental treatment conditions 24
2.1.4 Raman spectroscopy 25
2.1.5 SEM/EDS analysis 26
2.1.6 Microhardness testing 27
2.2 Computational methodology 28
2.2.1 Physicochemical model and adaptation to saliva 28
2.2.2 Equilibrium calculation, activity correction and HAp saturation . . 29

2.2.3 Model verification and saliva baseline definition 31
2.2.4 pH-dependent saturation and sensitivity analyses 32
2.2.5 Literature-based saliva scenarios and Ca–PO_4 interaction analysis . 33
2.2.6 Exploratory multidimensional uncertainty analysis 34
2.2.7 Thermodynamic characterization of the experimental treatment solutions 35

3 Results 37
3.1 Experimental Results 37
3.1.1 Baseline Raman characterization 37
3.1.2 Baseline SEM/EDS characterization 38
3.1.3 Baseline microhardness characterization 39
3.1.4 Raman characterization after the experimental treatments 39
3.1.5 SEM characterization after the experimental treatments 41
3.2 Computational Results 45
3.2.1 Model verification and saliva baseline 45
3.2.2 pH-dependent saturation and sensitivity analysis 46
3.2.3 Literature-based unstimulated and stimulated saliva scenarios . . . 48
3.2.4 Calcium–phosphate interaction maps 48
3.2.5 Multidimensional uncertainty analysis 50
3.2.6 Thermodynamic characterization of the experimental treatment solutions 52

4 Discussion 56
4.1 Summary of findings 56
4.2 Assumptions and intrinsic limitations 58
4.3 Future experimental and computational developments 60

5 Conclusions 62

A Exploratory quasi-equilibrium response to a plaque-derived pH challenge 64
.1 Exploratory plaque-derived acidification stress test 64

References 68

Abstract

Dental caries is a highly prevalent and multifactorial disease affecting the mineralized tissues of the tooth, particularly enamel and dentin. Its development is governed by the dynamic balance between enamel demineralization and remineralization, which determines whether mineral loss can be recovered or progresses toward tissue damage. Under physiological conditions, saliva plays a protective role by buffering acids and supplying calcium and phosphate ions that contribute to enamel mineral homeostasis. When bacterial metabolism within dental plaque causes a sufficient decrease in local pH, the surrounding fluid may become undersaturated with respect to hydroxyapatite, thermodynamically favoring mineral dissolution and progressive enamel demineralization.

In this context, this thesis aimed to combine experimental and computational approaches to investigate the properties of dental enamel and the stability of hydroxyapatite under conditions relevant to saliva and to the experimental treatments.

The experimental part focused on bovine enamel samples. Samples were prepared by cutting, epoxy embedding, grinding and polishing to obtain flat surfaces suitable for characterization. The untreated samples were initially characterized by Raman spectroscopy, scanning electron microscopy coupled with energy-dispersive X-ray spectroscopy (SEM/EDS), and microhardness testing, providing a baseline reference for subsequent experimental treatments. Additional specimens were then subjected for six days to demineralizing, remineralizing, or dry control conditions and subsequently examined by Raman spectroscopy and SEM.

Baseline Raman spectra showed the characteristic phosphate- and carbonate-related vibrational features of dental apatite. SEM/EDS provided information on enamel surface morphology and elemental composition, while microhardness measurements characterized the initial mechanical response of the enamel surface. Following the experimental treatments, the characteristic apatite Raman fingerprint remained detectable under all investigated conditions, although differences in spectral intensity were observed. SEM imaging further revealed qualitative differences in surface morphology and in the organization of mineral features among the Demin, Remin, and Dry conditions.

In parallel, an existing equilibrium model originally developed for interstitial-fluid mineral chemistry was adapted to saliva-like ionic compositions and implemented in MATLAB to investigate hydroxyapatite saturation as a function of pH and ionic composition. Literature-based concentrations of the main salivary ions were used to assess equilibrium

speciation and hydroxyapatite saturation. The computational analysis included model verification, evaluation of the effect of pH on saturation, sensitivity analyses for individual ions, saliva-relevant physiological scenarios, calcium–phosphate saturation maps, and an exploratory multidimensional uncertainty analysis.

The simulations showed that the system shifted from hydroxyapatite undersaturation to supersaturation at approximately **pH 5.15** under the reference saliva-like conditions and showed that the position of this transition is influenced by ionic composition, particularly calcium and phosphate availability. Application of the equilibrium framework to the experimental treatment solutions further indicated marked hydroxyapatite undersaturation under the acidic demineralizing condition, whereas the modeled neutral remineralizing condition was predicted to be supersaturated with respect to hydroxyapatite.

Overall, this work establishes a preliminary experimental and computational framework for investigating enamel mineral stability under controlled chemical environments. By combining enamel characterization with saliva-dependent equilibrium modeling and thermodynamic interpretation of the experimental conditions, this study provides a basis for the design and interpretation of future *in vitro* investigations of enamel demineralization, remineralization, and artificial caries-like lesion formation.

Keywords: Dental caries; Dental enamel; Hydroxyapatite; Saliva; Demineralization; Remineralization; Raman spectroscopy; SEM/EDS; Microhardness; Computational modeling.

Chapter 1

Introduction

1.1 Tooth and dental enamel: structure and composition

1.1.1 Tooth anatomy and organization

Teeth are highly specialized organs of the oral cavity, characterized by the integration of mineralized and soft tissues with distinct structural, mechanical, and biological properties. Their organization enables them to withstand the mechanical forces generated during mastication while protecting the internal vital components of the tooth [1, 2]. In mammals, tooth morphology varies according to position and function within the dentition; nevertheless, teeth share a common structural organization consisting of a crown, exposed within the oral cavity, and one or more roots anchored within the alveolar bone [1].

From a structural perspective, the tooth is composed of four major tissues: **enamel, dentin, cementum, and dental pulp** [2] (Figure 1.1). Enamel forms the external covering of the anatomical crown and represents the hardest and most highly mineralized tissue of the tooth, providing resistance against the mechanical and chemical challenges of the oral environment [3]. Beneath the enamel, dentin constitutes the bulk of the tooth and provides mechanical support to the overlying enamel. The innermost region is occupied by the dental pulp, a vascularized and innervated connective tissue responsible for maintaining tooth vitality, while cementum covers the external surface of the root [1, 2].

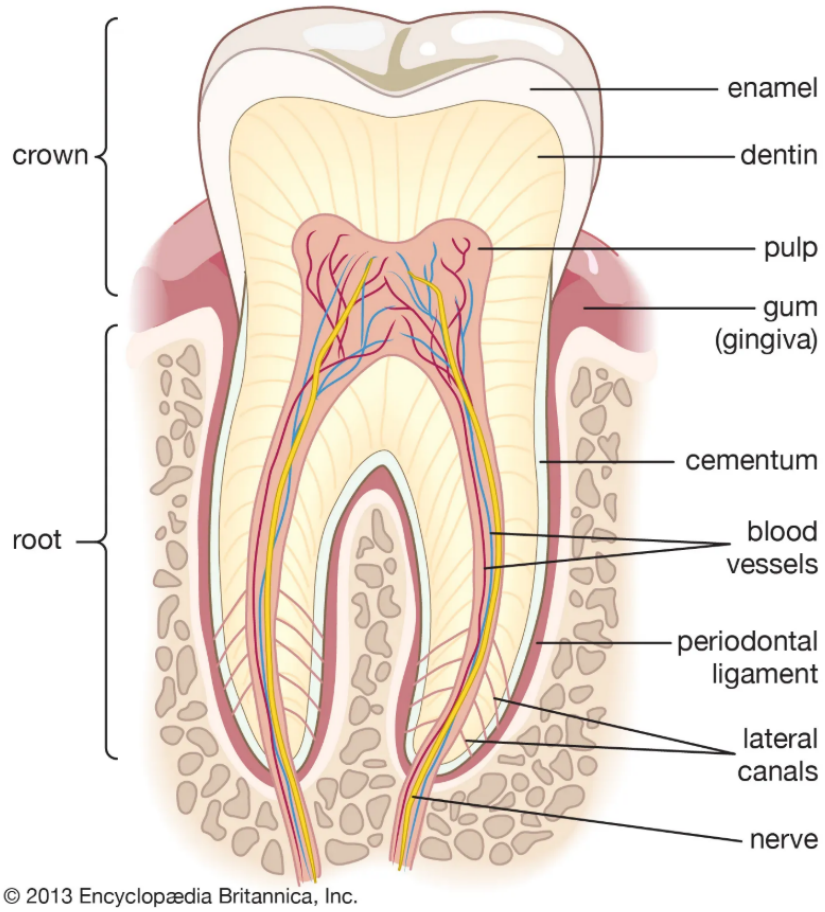


Figure 1.1: Schematic representation of human tooth anatomy and its main tissues.

The root is connected to the surrounding alveolar bone through the periodontal ligament, which contributes to tooth anchorage and the transmission of mechanical forces [1].

1.1.2 Dental enamel: formation, structure and organization

Dental enamel is a highly mineralized tissue characterized by a complex hierarchical organization extending from nanometre-sized mineral crystallites to micrometre-sized prisms and higher-order structural arrangements [4]. Unlike other mineralized dental tissues, mature enamel is acellular and cannot undergo physiological remodeling or regeneration after its formation [3, 5]. Its structural organization originates during amelogenesis, when specialized epithelial cells known as **ameloblasts** regulate the secretion of the extracellular matrix and the deposition and organization of the developing mineral phase [3, 6]. As enamel matures, most of the organic matrix is progressively removed while mineral content increases, resulting in the highly mineralized structure characteristic of mature enamel [3].

At the nanoscale, enamel is composed of elongated apatite crystallites that are highly oriented and organized rather than randomly distributed within the tissue. Mature enamel crystallites have reported cross-sectional dimensions of approximately 15–50 nm in thickness and 40–150 nm in width, with a considerably greater longitudinal dimension [4]. The organization and orientation of these crystallites provide the basis for the higher hierarchical levels of enamel structure.

At the micrometre scale, groups of aligned crystallites form **enamel prisms**, or **enamel rods**, which extend from the dentin–enamel junction (DEJ) toward the external enamel surface [3]. Each rod is formed by an ameloblast during amelogenesis and is surrounded by **interrod enamel**, which is similarly composed of mineral crystallites but differs primarily in their orientation [3]. At higher levels of organization, prisms may follow relatively parallel trajectories, forming **radial enamel**, or cross each other at different orientations, producing **decussating enamel**. Alternating groups of decussating prisms give rise to the characteristic **Hunter–Schreger bands (HSBs)** [4]. The hierarchical organization of enamel across these different length scales is illustrated in Figure 1.2.

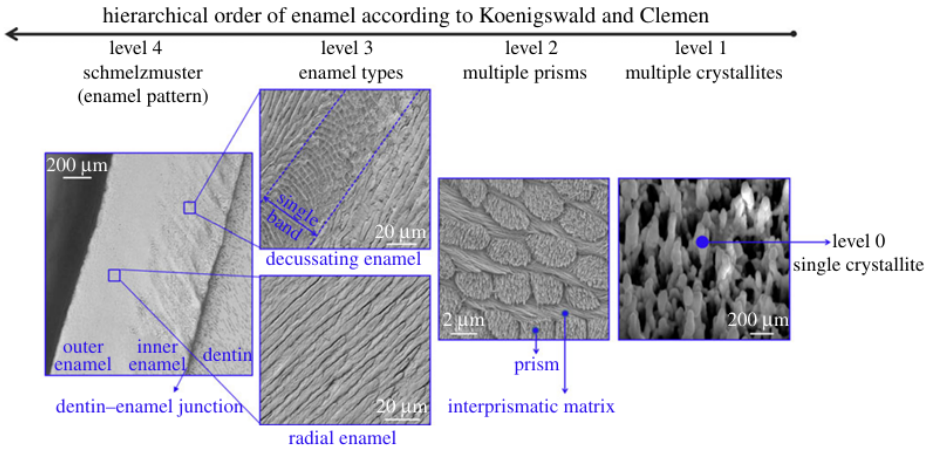


Figure 1.2: Hierarchical structural organization of bovine dental enamel, from individual crystallites to prisms and higher-order enamel patterns. Reproduced from Yilmaz et al. [4].

This hierarchical organization contributes to the characteristic mechanical properties of enamel, as the orientation and arrangement of crystallites and prisms influence stress distribution and crack propagation within the tissue [4].

1.1.3 Chemical and mineral composition of dental enamel

Dental enamel is distinguished from the other mineralized dental tissues by its exceptionally high inorganic content. Mature human enamel consists of approximately 95% mineral by weight, while the remaining fraction is represented by approximately 1–2% organic material and 2–4% water [3]. The predominance of the inorganic phase is responsible for the high hardness and stiffness of enamel, whereas the smaller organic and water fractions contribute to the overall properties of the tissue [7].

The mineral phase of mature enamel is predominantly composed of calcium phosphate in the form of biological apatite, structurally related to hydroxyapatite (HAp) [8]. Elemental analyses of human enamel consistently identify calcium (Ca) and phosphorus (P) as the predominant mineral elements [9] (Figure 1.3). In addition to calcium and phosphorus, enamel contains several minor constituents, including carbonate, sodium, magnesium, potassium, chloride, and fluoride [8]. Although present at lower concentrations, these constituents contribute to the chemical variability of the mineral phase.

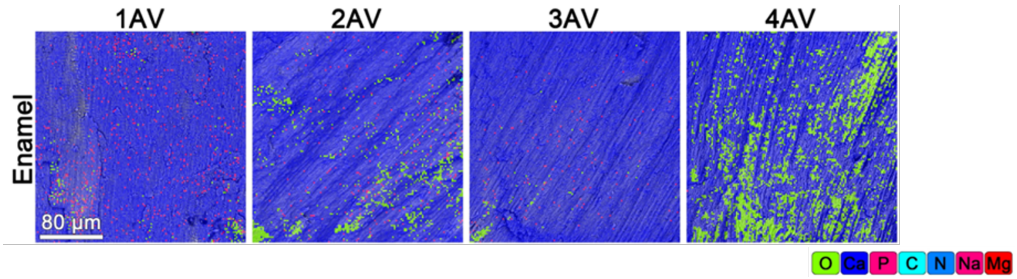


Figure 1.3: Elemental distribution maps of human dental enamel, showing the spatial distribution of O, Ca, P, C, N, Na, and Mg. Adapted from [9].

The distribution of these constituents is not uniform throughout the enamel thickness. Fluoride and chloride tend to occur at higher concentrations near the external enamel surface, whereas carbonate, sodium, and magnesium generally increase toward deeper enamel regions [8, 10]. These compositional gradients reflect processes occurring during enamel formation as well as post-eruptive interactions between the enamel surface and the oral environment [8].

The organic fraction of mature enamel is considerably smaller than that of dentin and bone and contains little or no collagen. It consists primarily of residual enamel-specific proteins and other organic components [7, 3]. Water represents an additional minor component of mature enamel and is present within the tissue in association with the mineral and organic phases [3].

1.1.4 Hydroxyapatite: structure and role in dental enamel

Hydroxyapatite (HAp) is a calcium phosphate mineral that represents the structural reference for the mineral phase of dental enamel. In its ideal stoichiometric form, hydroxyapatite has the chemical formula $Ca_{10}(PO_4)_6(OH)_2$ and a theoretical calcium-to-phosphorus (Ca/P) molar ratio of approximately 1.67 [11, 7]. Its crystalline structure provides the basic framework of the biological apatite present in dental enamel.

Hydroxyapatite crystallizes in a structure characterized by calcium ions, phosphate groups, and hydroxyl ions arranged in specific crystallographic positions. Two distinct calcium sites, commonly referred to as Ca(I) and Ca(II), are present within the lattice, while hydroxyl ions are arranged along channels parallel to the crystallographic c-axis [11] (Figure 1.4).

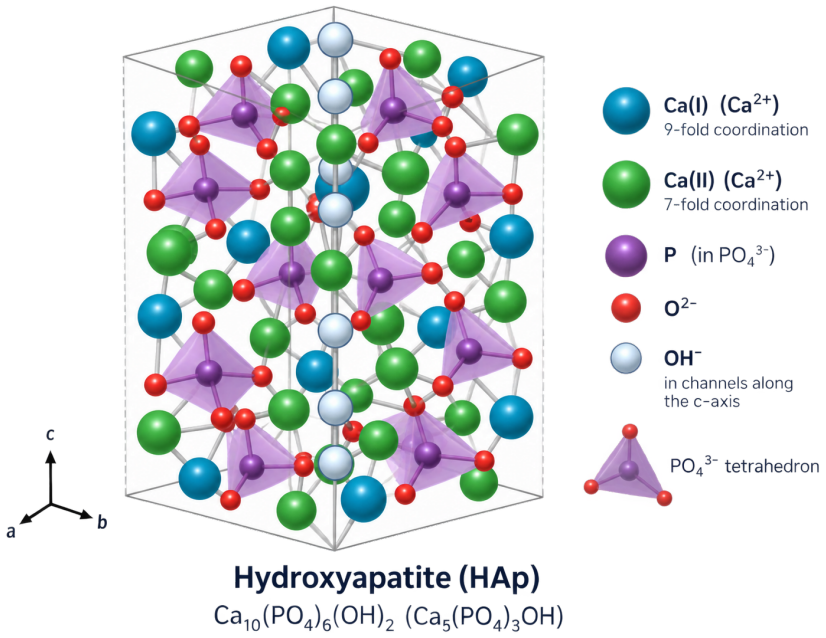


Figure 1.4: Schematic representation of the hydroxyapatite crystal structure, showing the structural positions of Ca(I), Ca(II), phosphate groups (PO_4), and hydroxyl groups (OH). AI-generated illustration created using ChatGPT (OpenAI).

The mineral present in dental enamel, however, should not be regarded as perfectly stoichiometric hydroxyapatite. Enamel mineral is more appropriately described as a biological apatite, characterized by ionic substitutions, vacancies, and deviations from the ideal calcium and hydroxyl content [8]. Consequently, its chemical composition may differ from that predicted for pure hydroxyapatite while retaining the characteristic apatite crystalline framework.

Several ionic substitutions can occur within biological apatite. Calcium sites may be partially occupied by ions such as sodium or magnesium, hydroxyl positions may accommodate fluoride or chloride, and carbonate can substitute within phosphate- or hydroxyl-related sites [7]. These substitutions contribute to the compositional variability of dental enamel and can influence the organization and stability of the mineral phase [8, 7].

1.1.5 Human and bovine enamel

Human enamel represents the most clinically relevant substrate for experimental studies aimed at investigating dental structure, mineralization, and caries-related processes. However, the use of extracted human teeth in laboratory research presents several practical and ethical limitations. Human dental specimens may be difficult to obtain in sufficient numbers and with comparable characteristics, and their collection and use require appropriate procedures for the management of human biological material. Moreover, donor-related factors such as age, biological history, previous exposure to the oral environment, restorations, or pre-existing dental alterations may introduce variability among specimens [12, 13].

For these reasons, bovine teeth are widely used as an alternative experimental substrate in dental research. They are readily available and can be collected in relatively large numbers, usually from animals slaughtered for food production, without the need to sacrifice animals specifically for experimental purposes [12, 14]. Bovine incisors also offer relatively large and flat enamel surfaces, which simplify specimen preparation and make it easier to obtain samples with standardized dimensions [12, 13, 15]. This makes them a practical choice for studies requiring several comparable enamel specimens under controlled experimental conditions.

Bovine enamel is commonly used as a model for human enamel because the two tissues share similar structural features. Both have a prismatic organization, with enamel prisms arranged either in parallel or in decussating patterns depending on their position within the tissue. In both substrates, decussating prisms can form Hunter–Schreger bands (HSBs), whereas parallel prism arrangements are observed in other enamel regions [16]. Despite these common organizational features, differences in prism and interprism architecture have been reported between the two species [16] (Figure 1.5).

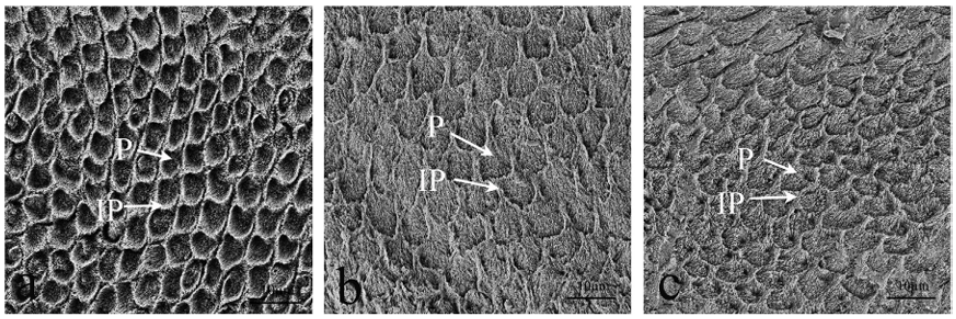


Figure 1.5: SEM micrographs comparing tangential sections of bovine and human enamel with parallel prisms: (a) bovine incisor, (b) human maxillary central incisor, and (c) human maxillary lateral incisor. P: prisms; IP: interprisms. Reproduced from [16].

Similarities between the two substrates also extend to their mineral composition. Calcium and phosphorus represent the predominant mineral elements in both human and bovine enamel, and comparative analyses have reported broadly similar chemical characteristics [17, 18, 14]. These similarities further support the use of bovine enamel as an experimental analogue of human enamel.

Despite their structural and compositional similarities, bovine and human enamel should not be considered identical. Differences in enamel thickness, prism and interprism organization, and physical and mechanical properties have been reported [16, 18, 15]. Such differences may influence the response of the two substrates under experimental conditions and should therefore be considered when results obtained using bovine enamel are interpreted in relation to human dental tissues [12, 13, 19].

Overall, bovine enamel represents a practical and reproducible experimental model that combines important structural and compositional similarities to human enamel with advantages in terms of availability, specimen size, and standardization [12, 16, 13].

1.2 Dental caries and enamel mineral dynamics

1.2.1 Definition and clinical relevance

Dental caries is one of the most prevalent chronic diseases affecting children and adults worldwide and represents a major global oral health problem [20, 13]. It affects the mineralized tissues of the tooth and develops through the interaction between the dental surface, microbial biofilm, and fermentable dietary carbohydrates. The metabolism of carbohydrates by cariogenic microorganisms results in the production of organic acids, creating local conditions that favor mineral loss from dental hard tissues [7, 13]. Dental caries is therefore currently regarded as a **multifactorial and dynamic disease** [7, 13], rather than solely as a process of irreversible tooth destruction.

Dental caries represents a considerable **public health burden** because of its high prevalence throughout the life course. According to data from the **2017 Global Burden of Disease study** [20], untreated caries in permanent teeth showed the highest prevalence among the 328 diseases and conditions evaluated, while its incidence ranked second. More than **one-third of the world's population** was reported to be living with untreated dental caries. In the primary dentition, untreated caries represents the most prevalent chronic condition of childhood, affecting approximately **514 million children worldwide** [20]. Despite advances in prevention, detection, and management, dental caries therefore remains a major challenge for oral healthcare worldwide.

The clinical manifestation of dental caries varies according to the severity and activity of the disease. Carious lesions may range from initial **non-cavitated enamel alterations** to progressively more extensive lesions involving structural breakdown and cavitation [20]. In its early stages, mineral loss can occur beneath a macroscopically intact enamel surface, producing a subsurface lesion [3, 21]. These initial alterations may become clinically visible as opaque, whitish areas commonly referred to as **white spot lesions (WSLs)** [21, 22]. With continued disease progression, the lesion may extend beyond enamel and involve the underlying dentin and, at advanced stages, the dental pulp [20] (Figure 1.6).

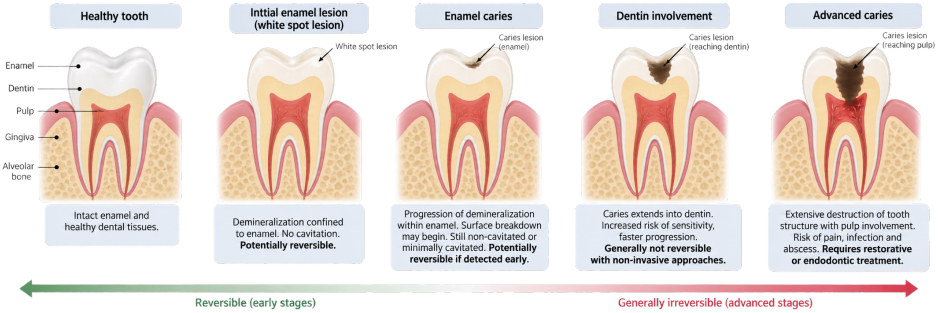


Figure 1.6: Schematic representation of the progression of dental caries, from healthy dental tissues to initial enamel lesions and progressively deeper involvement of dentin and pulp. AI-generated illustration created using ChatGPT (OpenAI).

The distinction between **non-cavitated and cavitated lesions** has important clinical implications. Early detection of carious lesions before surface cavitation allows disease

progression to be monitored and favors preventive, non-invasive, or micro-invasive management strategies [20]. Contemporary caries management has consequently shifted from an exclusively restorative approach toward strategies emphasizing **early detection, disease control, and preservation of dental tissues** [20].

1.2.2 Enamel demineralization and remineralization

The development of enamel caries is closely related to the dynamic balance between **demineralization and remineralization** of the enamel mineral phase. Demineralization refers to the loss of mineral ions from apatite crystals, whereas remineralization represents the restoration of mineral within partially demineralized enamel [7, 23]. Under physiological oral conditions, these opposing processes occur repeatedly, and their relative predominance determines the net mineral state of enamel. When mineral loss exceeds mineral recovery over time, the balance shifts toward **net demineralization**, promoting the development of an enamel carious lesion [7, 21].

During **demineralization**, dissolution of the enamel mineral phase causes ions to be released from apatite crystals into the surrounding environment [7, 21]. In particular, **calcium and phosphate ions** are progressively lost from the mineral phase. The aqueous component of enamel allows dissolved species to diffuse through the tissue, enabling the outward movement of mineral ions [7]. As this process continues, the mineral content of enamel decreases and its porosity increases [21].

Importantly, initial mineral loss does not necessarily represent an irreversible alteration. As long as a residual mineral framework is preserved, the process may be counteracted by **remineralization** [7]. During remineralization, mineral ions available in the surrounding environment are incorporated into partially demineralized enamel. Calcium and phosphate are particularly important because they provide the ionic constituents required for mineral deposition and recovery of the apatite phase [7, 21]. Rather than representing the biological regeneration of newly formed enamel, this process involves mineral deposition within previously demineralized regions and recovery of the residual mineral structure [7].

Several experimental approaches have been investigated to enhance enamel remineralization by increasing the availability of calcium and phosphate ions or by promoting mineral deposition within demineralized enamel. These include fluoride-based treatments, casein phosphopeptide–amorphous calcium phosphate (CPP–ACP) systems, calcium-phosphate formulations, and bioactive glass-based materials [24, 25, 26, 27]. Other studies have also evaluated remineralizing agents in artificially demineralized enamel and white spot lesions, showing that different formulations can promote partial recovery of the mineralized tissue under controlled experimental conditions [28, 29, 22].

The mineral state of enamel therefore reflects the cumulative balance between these two opposing processes. When remineralization compensates for mineral loss, the mineral integrity of enamel can be maintained or partially recovered. Conversely, repeated episodes in which demineralization predominates result in a progressive net loss of mineral and favor caries progression [7, 21] (Figure 1.7).

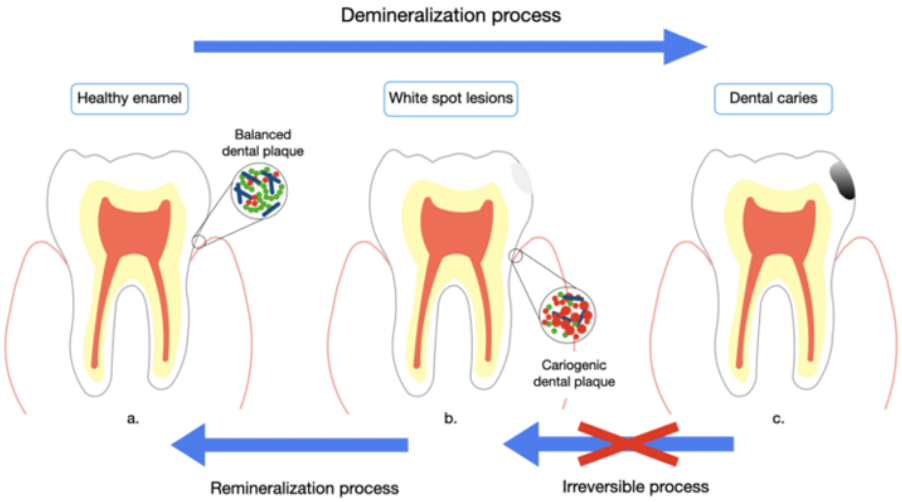


Figure 1.7: Schematic representation of the dynamic balance between enamel demineralization and remineralization and its relationship with the progression of dental caries. Reproduced from [21].

1.2.3 Role of pH in enamel mineral balance

pH is one of the main physicochemical factors influencing the stability of the enamel mineral phase. Because enamel apatite is in contact with an aqueous environment, variations in hydrogen ion concentration modify the chemical conditions governing the equilibrium between the solid mineral and the dissolved ionic species. A decrease in pH favors mineral dissolution, whereas an increase in pH reduces the tendency of enamel apatite to dissolve [3, 7].

The effect of pH on enamel mineral stability is closely related to the composition of the apatite phase. Hydroxyapatite contains calcium, phosphate, and hydroxyl ions, and its stability depends on the equilibrium established between these ions and the surrounding solution [3, 7]. As pH decreases, the higher concentration of hydrogen ions promotes the protonation of phosphate species, reducing the amount of phosphate available for the apatite equilibrium. At the same time, hydroxyl ion concentration also decreases. Together, these changes favor mineral dissolution and the release of calcium and phosphate ions from enamel into the surrounding solution [7].

In the oral environment, organic acids produced within dental biofilm can cause **transient reductions in pH** at the tooth surface, creating conditions that favor apatite dissolution [7, 13, 30]. Enamel may therefore experience repeated fluctuations in pH, whose magnitude, duration, and frequency influence their cumulative effect on the mineral phase [7, 30].

A pH of approximately **5.5** is commonly reported as a reference **critical pH** for enamel hydroxyapatite, below which mineral dissolution becomes increasingly favorable under typical oral conditions [21, 13]. However, this value should not be interpreted as a fixed or universal threshold. The stability of enamel apatite depends not only on pH but also on the chemical composition of the surrounding environment, particularly the concentrations of mineral ions such as calcium and phosphate [7, 31]. Consequently, identical pH values

may not necessarily correspond to the same tendency toward mineral dissolution under different ionic conditions.

Therefore, although pH is a major determinant of enamel mineral stability, **it cannot be considered independently of the chemical composition of the surrounding environment**. The tendency of the mineral phase to remain stable or undergo dissolution also depends on the ionic conditions of the aqueous phase surrounding the enamel [7].

1.3 Saliva and enamel mineral homeostasis

1.3.1 Human saliva: composition, functions and buffering capacity

Saliva is a complex biological fluid that continuously interacts with the teeth and oral tissues and contributes to the maintenance of oral homeostasis. Whole saliva present in the oral cavity results from the combined secretions of the major and minor salivary glands and contains both inorganic and organic components. Its composition is not constant but varies according to several factors, including glandular origin, stimulation, and salivary flow rate [32, 33, 34].

Saliva consists predominantly of water, which acts as a solvent for a wide range of **inorganic ions and organic molecules**. Its inorganic fraction includes electrolytes such as sodium (Na^+), potassium (K^+), chloride (Cl^-), bicarbonate (HCO_3^-), calcium (Ca^{2+}), phosphate species, and smaller amounts of other ions such as magnesium (Mg^{2+}) [35, 33, 36]. The organic fraction includes proteins, glycoproteins, enzymes, mucins, and other molecules that contribute to the characteristic physicochemical and biological properties of saliva [32].

This complex composition allows saliva to perform several functions within the oral cavity. It contributes to **lubrication and hydration** of oral surfaces, facilitates mastication and swallowing, participates in the clearance of food residues and microorganisms, and provides components involved in antimicrobial defense [32, 37]. Salivary macromolecules also interact with dental surfaces and contribute to the formation of the **acquired salivary pellicle**, which forms an interface between enamel and the surrounding oral environment [32].

Saliva may be considered under **unstimulated** or **stimulated** conditions. Unstimulated saliva refers to saliva secreted under resting conditions, whereas stimulated saliva is produced following stimulation of salivary flow, for example through mastication [38].

Another important protective function of saliva is its **buffering capacity**, namely its ability to resist changes in pH following the addition or production of acids or bases. This function is mainly associated with the **bicarbonate buffering system**, particularly in stimulated saliva, while phosphate species and salivary proteins also contribute to the overall buffering capacity [33]. Bicarbonate concentration increases with salivary flow rate, making the buffering capacity of saliva dependent, to some extent, on the rate of secretion [33].

1.3.2 Salivary ions and enamel mineral equilibrium

The inorganic constituents of saliva contribute to the mineral environment surrounding dental enamel. Among the different salivary ions, **calcium and phosphate are particularly relevant**, as they represent major ionic constituents of the apatite mineral phase. Their presence in the oral fluid contributes to the chemical equilibrium established between saliva and enamel [7].

Calcium and phosphate in saliva can occur in different chemical forms. Calcium is present both as free Ca^{2+} and in association with other salivary constituents, whereas phosphate is distributed among different protonated species, mainly $H_2PO_4^-$ and HPO_4^{2-} under physiological conditions. The relative distribution of phosphate species is strongly influenced by **pH**. Consequently, the chemical behavior of calcium and phosphate depends not only on their total concentrations, but also on their **speciation and availability in solution** [39].

Other inorganic constituents of saliva may also influence the chemical environment surrounding enamel through their interactions with the principal mineral ions. Saliva should therefore be considered as a **multicomponent ionic system**, in which the behavior of calcium and phosphate is influenced by the overall composition and physicochemical conditions of the oral fluid [35, 39].

1.3.3 Hydroxyapatite saturation and dissolution equilibrium

The stability of enamel hydroxyapatite is closely related to the physicochemical composition of the surrounding oral fluid. In saliva, the activities of calcium, phosphate, and hydroxyl ions determine the degree of saturation with respect to hydroxyapatite, providing a thermodynamic measure of the tendency of the mineral phase to remain stable or undergo dissolution [39, 40, 41].

Using the half-unit representation of hydroxyapatite, $Ca_5(PO_4)_3OH$, the dissolution equilibrium can be written as [39]:

$$Ca_5(PO_4)_3OH \rightleftharpoons 5Ca^{2+} + 3PO_4^{3-} + OH^- \tag{1.1}$$

The corresponding ion activity product (IAP) is expressed as [39, 40]:

$$IAP = (a_{Ca^{2+}})^5 \left(a_{PO_4^{3-}}\right)^3 (a_{OH^-}) \tag{1.2}$$

where a_i represents the activity of each ionic species. Ionic activity reflects the effective chemical contribution of an ion in solution and depends on both its concentration and its activity coefficient. The activity coefficient is in turn influenced by the **ionic strength** of the solution, which reflects the concentration and electrical charge of the ions present in the aqueous environment [42]. The use of ionic activities is therefore particularly relevant for describing mineral equilibria in a multicomponent fluid such as saliva [40]. The IAP integrates the contributions of the ionic species directly involved in hydroxyapatite equilibrium and is consequently influenced by the chemical composition of the surrounding salivary environment [39].

The saturation state of a solution with respect to hydroxyapatite is determined by the relationship between the IAP and the solubility product of hydroxyapatite, K_{sp} [43].

When the ion activity product is lower than the solubility product, the solution is **undersaturated** with respect to hydroxyapatite and mineral dissolution is thermodynamically favored. At equilibrium, the ion activity product corresponds to the solubility product. Conversely, when the ion activity product exceeds the solubility product, the solution is **supersaturated**, and precipitation or crystal growth is thermodynamically favored [43].

The saturation state is strongly influenced by pH, since changes in pH affect both hydroxyl activity and phosphate speciation. A decrease in pH reduces hydroxyl activity and modifies the distribution of phosphate species, thereby affecting the ion activity product and the saturation state of the solution. Consequently, hydroxyapatite saturation reflects the combined effects of pH, calcium, and phosphate, rather than any of these parameters considered independently [39, 44, 45].

In the oral environment, the degree of saturation of saliva with respect to hydroxyapatite therefore provides a useful physicochemical framework for understanding the conditions that favor enamel mineral stability or dissolution. However, the saturation state describes the thermodynamic tendency of the system and does not, by itself, determine the actual rate at which mineral dissolution or precipitation occurs.

1.3.4 Simplified saliva-like models of the oral environment

The complex and variable composition of natural saliva represents a challenge for the controlled investigation of physicochemical processes occurring in the oral environment. Salivary composition can vary considerably among individuals and within the same individual depending on factors such as glandular origin, stimulation, and flow rate. For this reason, simplified saliva-like systems are commonly used to reproduce selected characteristics of the oral fluid under more controlled and reproducible conditions [32, 35].

One approach is the use of **artificial saliva**, consisting of aqueous formulations designed to reproduce selected components and properties of natural saliva. These formulations commonly include inorganic constituents such as sodium, potassium, chloride, bicarbonate, calcium, magnesium, and phosphate species, although their concentrations and combinations vary according to the purpose of the model and the characteristics of the oral environment that are intended to be represented [32, 35]. For example, Sato et al. developed an artificial saliva formulation based on experimentally determined concentrations of major inorganic constituents in natural human saliva [35].

The use of simplified saliva-like systems allows parameters such as ionic composition, pH, and mineral ion concentrations to be defined and varied under controlled conditions. Such systems can therefore provide a reproducible environment for investigating physicochemical processes at the tooth–fluid interface and the conditions associated with enamel mineral stability and dissolution [35].

However, artificial saliva remains a simplified representation of the natural oral environment. Depending on the formulation, proteins, enzymes, mucins, and other organic components may be absent or only partially represented, and the biological variability of natural saliva cannot be fully reproduced [32]. Artificial saliva should therefore be regarded as a controlled physicochemical approximation of oral fluid rather than a complete substitute for natural human saliva.

1.4 Shared physicochemical principles of hydroxyapatite equilibrium in biological fluids

Bone and dental enamel are biologically and structurally distinct mineralized tissues. Bone is a collagen-rich and continuously remodeling tissue, whereas mature enamel contains little or no collagen, is considerably more highly mineralized, and does not undergo physiological remodeling. Despite these differences, the inorganic phase of both tissues is predominantly based on **biological apatite**, a calcium phosphate mineral related to hydroxyapatite [7].

The presence of an apatite-based mineral phase establishes an important physicochemical feature shared by these tissues: mineral stability depends on the chemical environment surrounding the solid phase. In bone, the mineralized matrix is in contact with **bone interstitial fluid (ISF)**, an aqueous ionic environment in which calcium, phosphate, carbonate, sodium, potassium, magnesium, and chloride participate in multiple chemical equilibria. The distribution of these species, together with pH and ionic interactions, influences the availability of ions involved in hydroxyapatite formation and the saturation state of the surrounding fluid [46, 42].

Dental enamel is exposed to a different biological environment. Following tooth eruption, its external mineral surface is continuously in contact with **saliva**, whose composition and physiological functions differ from those of bone interstitial fluid. Nevertheless, saliva is also an aqueous multicomponent ionic system containing calcium, phosphate, carbonate species, sodium, potassium, magnesium, and chloride, among other constituents. As discussed in the previous sections, the equilibrium between enamel mineral and saliva is influenced by pH, ionic composition, ion speciation, and the resulting degree of saturation with respect to apatite [33, 39].

Thus, bone–ISF and enamel–saliva systems should not be considered biologically equivalent. Their tissue organization, surrounding fluids, regulatory mechanisms, and characteristic physicochemical conditions are different. However, at the level of **mineral–solution equilibrium**, both involve an apatite-based solid phase interacting with an aqueous ionic environment containing several of the same major mineral-related ionic components, although at different concentrations and under different physiological conditions. In both cases, changes in pH and ionic availability can alter ion speciation and activity and consequently modify the thermodynamic conditions governing hydroxyapatite stability, dissolution, or precipitation [42, 39].

These common physicochemical principles provide a general framework for studying hydroxyapatite equilibrium in different biological environments, while the specific ionic composition and biological context of each system must be considered independently.

1.5 Rationale and objectives of the study

1.5.1 Scientific gap

Enamel demineralization is governed by the interaction between the mineral phase of the tooth and the surrounding oral environment. As discussed in the previous sections, acidic conditions promote hydroxyapatite dissolution, but the tendency of the mineral phase toward stability or dissolution depends not only on pH, but also on the ionic composition of the surrounding fluid, ion speciation, ionic activity, and the resulting saturation state.

Experimental models provide a controlled approach for reproducing enamel demineralization and directly characterizing the associated alterations in the mineralized tissue. Techniques such as Raman spectroscopy and scanning electron microscopy coupled with energy-dispersive X-ray spectroscopy (SEM/EDS) can provide information on mineral composition and structural changes, while mechanical measurements can contribute to the characterization of enamel properties.[47, 4, 9, 48] However, experimental characterization of the solid tissue does not directly describe the physicochemical conditions of the surrounding solution that determine whether hydroxyapatite dissolution is thermodynamically favored.

Conversely, physicochemical modelling can describe the equilibrium distribution of ionic species and evaluate the saturation state of an aqueous environment with respect to hydroxyapatite. Previous models developed for bone interstitial fluid have demonstrated how pH, ionic composition, ion speciation, and activity influence hydroxyapatite equilibrium under biologically relevant conditions [46, 42]. Nevertheless, the environment surrounding dental enamel differs substantially from bone interstitial fluid, since the external enamel surface interacts with saliva, a distinct multicomponent biological fluid characterized by its own ionic composition and physiological variability.

A complementary perspective is therefore needed to relate the experimental characterization of enamel mineral alterations to the physicochemical conditions of the surrounding aqueous environment that govern hydroxyapatite stability. Experimental analysis describes the changes occurring in the mineralized tissue, whereas physicochemical modelling can investigate the chemical conditions that favor mineral stability or dissolution. Considering these two levels together may therefore provide a more complete framework for studying enamel demineralization.

The goal of this thesis was therefore to investigate enamel mineral stability through complementary experimental and computational approaches. Experimentally, bovine enamel was used as a controlled model for baseline characterization and for the investigation of its response to demineralizing, remineralizing, and dry control conditions.

In parallel, a previously established physicochemical framework for hydroxyapatite equilibrium was adapted to a saliva-like ionic environment in order to investigate the effects of pH and ionic composition on hydroxyapatite saturation. Finally, the same framework was applied on a preliminary basis to the experimental treatment solutions, providing an exploratory physicochemical characterization of the conditions used in the experimental protocol.

1.5.2 Specific objectives

This thesis was guided by the following primary research question:

How do acidic conditions and variations in the surrounding ionic environment influence enamel mineral stability, and how can experimental characterization and physicochemical modelling provide complementary information on this process?

To address this question, the work was structured around the following specific objectives:

- **Preparation and baseline characterization of bovine enamel:** to prepare standardized bovine enamel specimens and characterize their initial structural, compositional, and mechanical properties using Raman spectroscopy, SEM/EDS, and Vickers microhardness measurements.
- **Controlled experimental treatment of enamel:** to investigate the response of bovine enamel to controlled demineralizing, remineralizing, and dry control conditions, evaluating changes in its mineral and surface characteristics relative to untreated reference enamel.
- **Adaptation of a physicochemical model to saliva:** to adapt a previously established hydroxyapatite equilibrium framework, originally developed for bone interstitial fluid, to a saliva-like multicomponent ionic environment and evaluate its applicability for the analysis of salivary mineral equilibrium.
- **Analysis of hydroxyapatite saturation under salivary conditions:** to investigate the influence of pH, ionic composition, ion speciation, and ionic activity on hydroxyapatite saturation and to identify the conditions associated with the transition between supersaturation and undersaturation.
- **Evaluation of salivary ionic variability:** to assess the sensitivity of hydroxyapatite equilibrium to physiologically relevant variations in salivary composition, with particular attention to calcium, phosphate, and carbonate, as well as to the combined effects of multiple ionic components and different salivary conditions.
- **Preliminary thermodynamic characterization of the experimental treatment solutions:** to apply the physicochemical model to the demineralizing and remineralizing solutions used in the experimental protocol and obtain an exploratory characterization of their saturation state with respect to hydroxyapatite, providing a preliminary physicochemical interpretation of the aqueous treatment conditions used experimentally.

Chapter 2

Materials and Methods

2.1 Experimental methodology

The experimental work was designed to characterize bovine dental enamel and investigate the effects of controlled mineral exposure under *in vitro* conditions. Bovine enamel specimens were prepared through cutting, embedding, grinding, and polishing. Untreated reference specimens were used for baseline characterization by Raman spectroscopy, scanning electron microscopy coupled with energy-dispersive X-ray spectroscopy (SEM/EDS), and Vickers microhardness testing. Separate specimens were assigned to three experimental conditions for 6 days: a demineralization condition at pH 4.0 (Demin), a pH 7.0 mineral solution condition (Remin), and a dry control condition (Dry). The exposed specimens were subsequently characterized to evaluate differences among the experimental conditions and in relation to the untreated reference enamel.

2.1.1 Bovine enamel specimens

Bovine molars and premolars provided by **Prof. Robert E. Burrell, Department of Biomedical Engineering, University of Alberta** were used for the experimental study. The teeth were received within sections of bovine jaw, with residual surrounding tissues still present. Upon receipt, the specimens were stored in a laboratory freezer and maintained frozen until further processing.

Prior to sample preparation, the specimens were removed from frozen storage and suitable teeth were selected for the experimental study. The selected teeth were subsequently transferred to the **Thin Section Laboratory, Department of Earth and Atmospheric Sciences, University of Alberta**, where the enamel specimens were prepared as described in Section 2.1.2.

2.1.2 Sample preparation: cutting, embedding, grinding and polishing

The preparation of bovine enamel specimens involved a sequence of **cutting, epoxy embedding, grinding, and polishing** steps. The overall procedure was developed to

obtain small and mechanically stable specimens with a flat and accessible enamel surface suitable for the subsequent experimental characterization.

Cutting of bovine teeth

The bovine molars and premolars initially consisted of relatively large tooth and jaw sections and therefore required progressive sectioning before further preparation. Cutting was performed at the **Thin Section Laboratory, Department of Earth and Atmospheric Sciences, University of Alberta**, using a rotating cutting wheel. The orientation of each cut was selected according to the region of interest, with the aim of obtaining small specimens containing an accessible portion of enamel while removing unnecessary surrounding dental tissue.

The main stages of the cutting procedure are shown in Figure 2.1. The specimens were progressively reduced from the original jaw sections to individual tooth portions and finally to small enamel-containing blocks suitable for embedding. Following sectioning, the resulting specimens were rinsed to remove debris generated during cutting and were allowed to dry before subsequent processing.

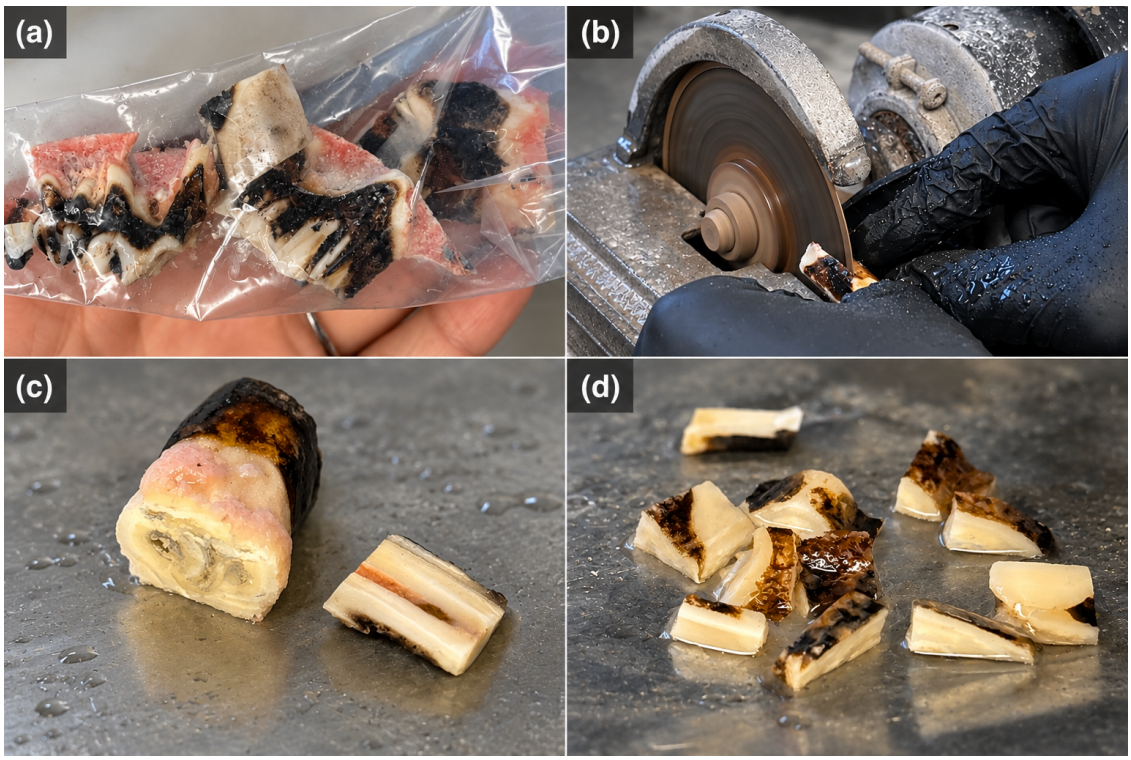


Figure 2.1: Preparation and sectioning of bovine teeth prior to embedding. (a) Bovine jaw sections containing molars and premolars before specimen preparation; (b) sectioning of the teeth using a rotating cutting wheel; (c) representative tooth portion obtained during progressive sectioning; (d) final small tooth blocks obtained after cutting, containing the enamel regions selected for subsequent preparation.

Epoxy embedding

Following cutting, the selected tooth blocks were individually embedded in epoxy resin to facilitate handling and provide mechanical support during the subsequent grinding and polishing procedures. Each specimen was positioned individually within a compartment of a flexible silicone mould, with particular attention to the orientation of the enamel region intended for analysis.

A transparent **two-component epoxy resin** was prepared and carefully introduced into the mould compartments until the tooth fragments were surrounded by liquid resin. The specimens were then left undisturbed under laboratory conditions for approximately **24 h** to allow complete curing of the epoxy. After polymerization, the individual blocks were removed from the silicone moulds, resulting in rigid transparent epoxy mounts containing the tooth specimens.

The different stages of the embedding procedure are illustrated in Figure 2.2. Embedding provided a stable support around the relatively small tooth fragments, facilitating their manipulation and allowing the selected enamel surface to be processed in a controlled manner during the following preparation steps.

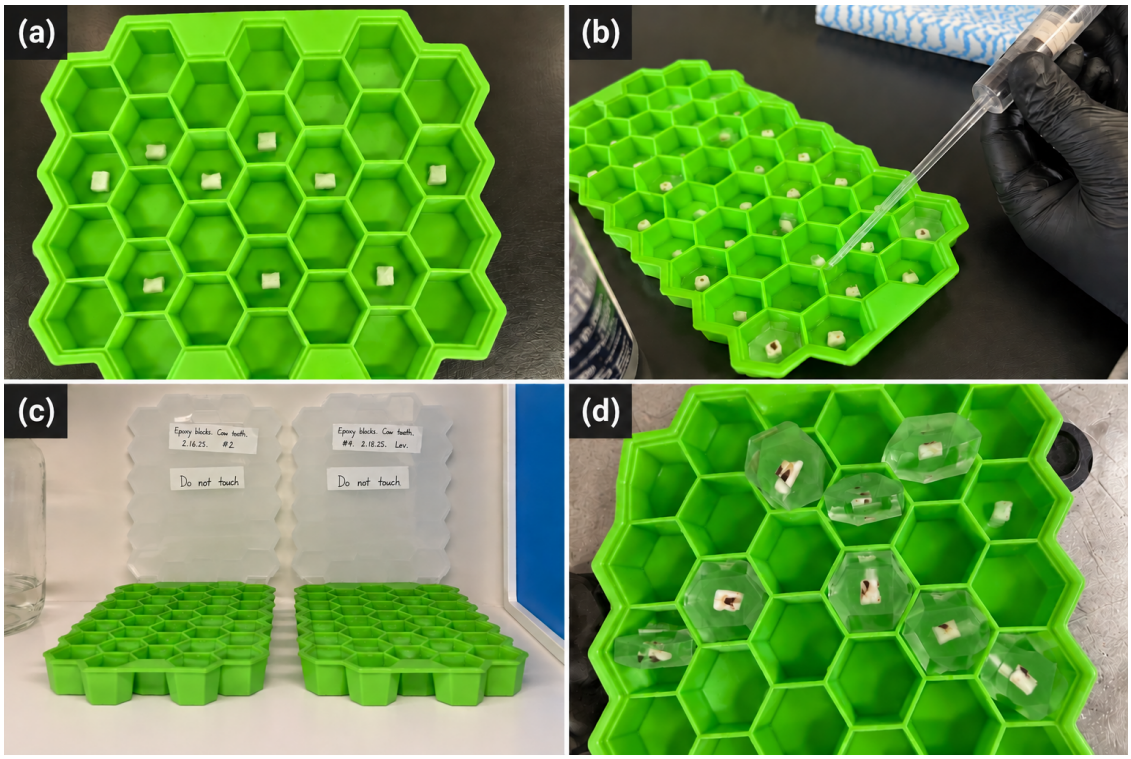


Figure 2.2: Epoxy embedding of the bovine tooth specimens. (a) Individual tooth fragments positioned inside separate compartments of the silicone mould; (b) addition of liquid epoxy resin around the specimens; (c) moulds maintained undisturbed for approximately 24 h to allow complete resin curing; (d) representative specimens after polymerization and removal from the mould, showing the tooth fragments incorporated within the transparent epoxy blocks.

Grinding and polishing

After complete curing, the epoxy-embedded specimens were returned to the Thin Section Laboratory for further processing. Since the initial embedding produced relatively large resin blocks around the tooth fragments, **excess epoxy was first mechanically removed** using a rotating cutting wheel. This trimming step reduced the dimensions of the blocks and allowed the embedded enamel region to be approached without unnecessarily removing dental tissue.

The specimens subsequently underwent **grinding** to progressively flatten the exposed surface and remove irregularities remaining from the cutting and embedding procedures. Grinding was performed using a rotating grinding surface, progressively exposing the region of interest and producing a more uniform specimen surface.

Additional local surface finishing was performed using a handheld rotary tool when necessary to remove residual material and refine the geometry of the individual specimens. Particular care was taken during these steps to maintain the enamel region intended for subsequent characterization.

Finally, the exposed surfaces were polished using a commercial diamond polishing paste. The polishing step was performed to reduce scratches and surface irregularities produced during the preceding mechanical preparation and to obtain a smooth and homogeneous enamel surface.The principal stages of this final preparation are illustrated in Figure 2.3.

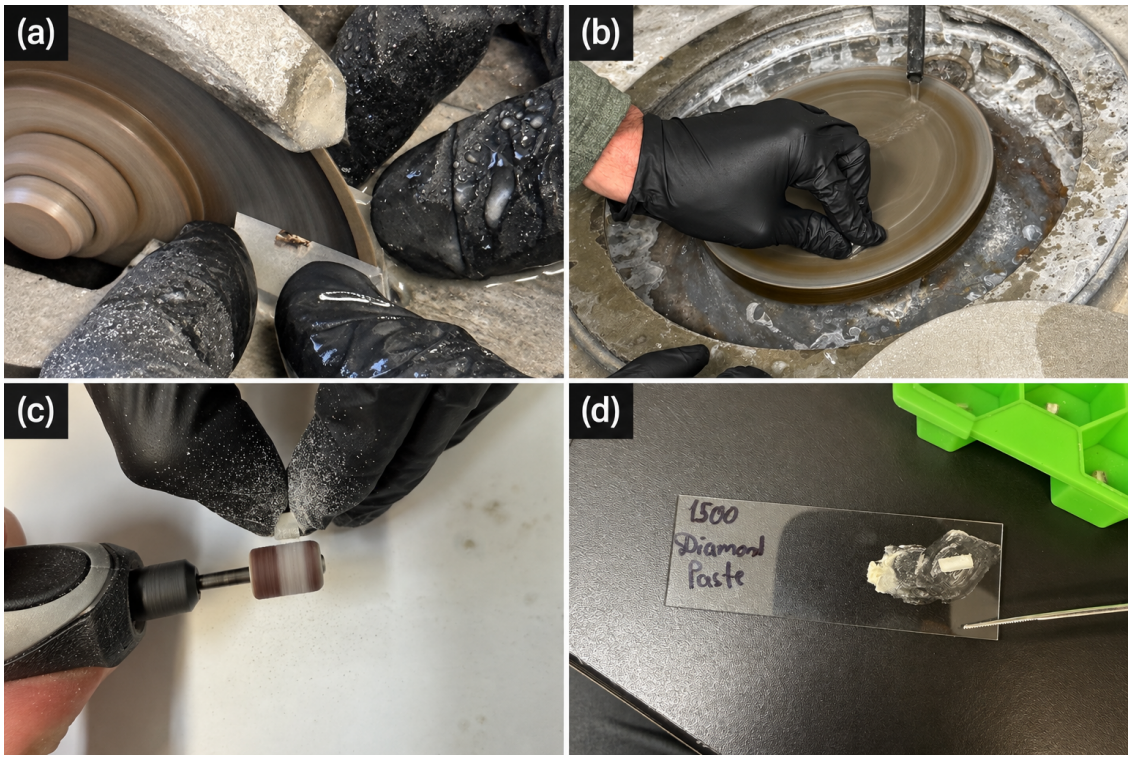


Figure 2.3: Grinding and polishing of epoxy-embedded bovine enamel specimens. (a) Mechanical trimming of the cured epoxy block to remove excess resin and approach the embedded tooth specimen; (b) grinding of the specimen using a rotating grinding surface to flatten and progressively expose the region of interest; (c) local surface finishing using a handheld rotary tool; (d) final polishing using a commercial diamond paste to obtain a smooth enamel surface suitable for subsequent characterization.

The resulting epoxy-mounted specimens presented an exposed, flat, and polished enamel surface suitable for the subsequent **Raman spectroscopy, scanning electron microscopy coupled with energy-dispersive X-ray spectroscopy (SEM/EDS), and microhardness measurements**.

2.1.3 Experimental treatment conditions

To investigate the response of enamel under different mineral conditions, a mineral solution containing calcium, phosphate, bicarbonate, sodium, potassium, and chloride ions was prepared. The same initial formulation was used to obtain the demineralization and remineralization solutions, thereby maintaining a comparable ionic environment while varying the pH conditions.

The solution was prepared under continuous magnetic stirring, starting from 160 mL of distilled water. The salts were sequentially added according to the amounts reported in Table 2.1. Specifically, 2.50 g of KCl, 0.55 g of NaCl, 0.060 g of $CaCl_2{\cdot}2H_2O$, 0.142 g of Na_2HPO_4, and 0.252 g of $NaHCO_3$ were dissolved. Complete dissolution of each compound was allowed before addition of the subsequent salt.

Table 2.1: Composition of the mineral solution used for the preparation of the demineralization and remineralization solutions.

Compound	Amount	Main ionic contribution
KCl	2.50 g	K^+, Cl^-
NaCl	0.55 g	Na^+, Cl^-
$CaCl_2 \cdot 2H_2O$	0.060 g	Ca^{2+}, Cl^-
Na_2HPO_4	0.142 g	Na^+, phosphate
$NaHCO_3$	0.252 g	Na^+, HCO_3^-

After complete dissolution of the salts, the prepared solution was divided into two portions to obtain the demineralization solution and the corresponding remineralization solution. For the demineralization condition (Demin), lactic acid was added to obtain a final concentration of 100 mM. The pH was monitored using a pH meter and adjusted with sodium hydroxide (NaOH). The demineralization solution was adjusted to pH 4.0, whereas the remineralization solution (Remin), prepared without lactic acid, was adjusted to pH 7.0.

To limit microbial growth during the experimental period, a thymol stock solution was prepared by dissolving 0.2 g of thymol in 2 mL of 95% ethanol. After complete dissolution, thymol was added to the prepared solutions.

The enamel specimens were assigned to three experimental conditions. Specimens in the Demin condition were immersed in the pH 4.0 demineralization solution for 6 days, whereas specimens in the Remin condition were immersed in the pH 7.0 remineralization solution for the same period. A third condition, referred to as Dry, consisted of specimens maintained for 6 days without exposure to either solution and was used as the dry control condition. Following the 6-day period, the specimens were recovered for subsequent characterization.

2.1.4 Raman spectroscopy

Raman spectroscopy was employed to characterize the mineral phase of bovine enamel and to compare the spectral features of untreated reference specimens with those observed under the Demin, Remin, and Dry experimental conditions. Raman spectroscopy is a vibrational spectroscopic technique based on the inelastic scattering of monochromatic light resulting from the interaction between incident photons and molecular vibrations. While most incident photons undergo elastic Rayleigh scattering, a small fraction is scattered with a change in energy. This energy difference, expressed as the Raman shift in cm^{-1}, is related to the vibrational modes of the analyzed material and provides information on its molecular composition and structure [47].

Raman spectroscopy is particularly suitable for the characterization of mineralized dental tissues, as their spectra contain characteristic bands associated with the inorganic components of the tissue. In dental enamel, which is predominantly composed of carbonated apatite, the Raman spectrum is dominated by vibrational modes associated with the phosphate groups (PO_4^{3-}) of the apatite mineral phase [47, 49]. The most prominent enamel Raman band is located at approximately 959–960 cm^{-1} and is assigned to the ν_1 symmetric

stretching vibration of PO_4^{3-}. Additional phosphate-related bands are associated with the ν_2, ν_3, and ν_4 vibrational modes and occur in different regions of the Raman spectrum [47].

The phosphate-related Raman bands can therefore provide information on the mineral characteristics of enamel and are useful for investigating changes associated with caries and demineralization. Previous studies comparing sound and demineralized or carious enamel have reported changes in the relative intensities of phosphate-related Raman bands, reflecting modifications of the enamel mineral phase [47, 49, 50]. In particular, alterations in Raman spectral features following demineralization have been associated with changes in the morphology and/or orientation of enamel apatite crystallites [47].

Raman spectroscopy measurements were performed at the nanoFAB facility of the University of Alberta (Edmonton, AB, Canada) using a **Renishaw inVia Qontor Confocal Raman Microscope**. Spectra were acquired using a **633 nm excitation laser**, a **50× objective**, and a **1200 grooves/mm diffraction grating**. The acquisition time was set to **2 s**, with **10 accumulations** collected for each measurement.

For each enamel specimen, Raman spectra were acquired at **five different points** across the analyzed enamel surface in order to account for local variations in mineral composition. The spectra collected from the five measurement locations were subsequently averaged to obtain a representative spectrum for each specimen. The raw spectral data, consisting of Raman shift (cm^{-1}) and corresponding intensity values, were exported from the instrument and subsequently imported into **OriginPro software (OriginLab Corporation, Northampton, MA, USA)**. The resulting spectra were plotted and visually examined to identify the characteristic Raman bands of the enamel mineral phase and to allow comparison among the different experimental conditions.

Baseline Raman characterization was performed on two untreated bovine enamel specimens, BT0 and BT1, which had been previously prepared by the geology facilities at the University of Alberta. These specimens were not subjected to any subsequent experimental treatment and were used as untreated reference samples.

Raman spectroscopy was also performed on enamel specimens assigned to the three 6-day experimental conditions described above: **Demin (pH 4.0 demineralization solution), Remin (pH 7.0 mineral solution), and Dry (no solution exposure)**. The same acquisition and data-processing procedure was applied to all analyzed specimens, allowing comparison of their Raman spectral features across the different experimental conditions and with the untreated reference enamel.

2.1.5 SEM/EDS analysis

Scanning electron microscopy (SEM) was employed to investigate the surface morphology and microstructural features of the enamel specimens. SEM is based on the interaction of a focused electron beam with the specimen, generating signals that can be used to obtain high-resolution images of the sample surface. Owing to its high spatial resolution, SEM is particularly suitable for investigating the hierarchical microstructure of mineralized dental tissues, including enamel, across different length scales [4, 9].

SEM/EDS measurements were performed at the **nanoFAB facility of the University of Alberta (Edmonton, AB, Canada)** using a **Hitachi S-4800 field-emission**

scanning electron microscope (FESEM) equipped with an energy-dispersive X-ray (EDS) detector. Prior to analysis, the specimens were coated with a **15 nm gold layer** to reduce sample charging during electron-beam imaging. Different operating conditions were used for morphological imaging and elemental analysis. SEM imaging of the enamel surface was performed at an accelerating voltage of **5 kV** and a working distance of approximately **5 mm**, conditions selected for surface topography characterization.

SEM images were acquired at approximately 400×**,** 5,000×**,** 12,000×**, and** 100,000× magnification, corresponding to fields of view of approximately **100** μ**m, 10** μ**m, 4** μ**m, and 500 nm**, respectively. The use of progressively increasing magnifications allowed the enamel surface to be examined at different length scales, from overall surface morphology to finer microstructural features.

For EDS analysis, the accelerating voltage was increased to **15 kV**, with a working distance of approximately **15 mm**. EDS spectra were acquired from selected enamel regions to identify the elements present within the analyzed area. In addition, **elemental maps** were collected to visualize the spatial distribution of the detected elements across the enamel surface. The spectra and elemental maps generated by the EDS system were subsequently examined for characterization of the elemental composition of the specimens.

Untreated reference enamel was used for baseline SEM/EDS characterization, while post-exposure morphological characterization was performed by SEM after the 6-day experimental period.

2.1.6 Microhardness testing

Microhardness testing was performed to obtain a baseline characterization of the mechanical properties of dental enamel. The Vickers microhardness test is based on the indentation of the specimen surface using a diamond indenter under a defined load. After removal of the applied load, the two diagonals of the residual indentation are measured and used to determine the Vickers hardness number (VHN). Surface microhardness measurements provide a useful method for evaluating the local mechanical properties of enamel and have been employed to assess changes in enamel associated with mineral loss and recovery [48, 19].

Microhardness measurements were carried out using a **Vickers microhardness tester** available in the **Department of Mechanical Engineering at the University of Alberta (Edmonton, AB, Canada)**. The testing parameters were selected according to a previously reported protocol for surface microhardness analysis of dental enamel [48].

The measurements were performed using a **Vickers diamond indenter** with a test load of **100 g (HV0.1)** applied for a dwell time of **10 s**. Three indentations were performed on each specimen. Following each indentation, the two diagonals of the residual impression were measured by the instrument, and the corresponding Vickers hardness value was determined from the indentation dimensions.

The measurements were performed on **previously prepared enamel specimens provided by the geology facilities at the University of Alberta**. Microhardness testing

was used exclusively for the **baseline mechanical characterization of the enamel** and was not repeated following the subsequent experimental treatments.

2.2 Computational methodology

The computational part of the study was implemented in MATLAB and developed to investigate the physicochemical conditions governing hydroxyapatite stability in a saliva-like ionic environment. A previously established physicochemical equilibrium model was adapted to salivary composition and used to evaluate the effects of pH and ionic variability on hydroxyapatite saturation. The analysis included model verification, definition of a reference saliva composition, pH-dependent saturation calculations, sensitivity analyses, literature-based saliva scenarios, calcium–phosphate interaction maps, an exploratory multidimensional uncertainty analysis, and an exploratory thermodynamic characterization of the experimental treatment solutions.

2.2.1 Physicochemical model and adaptation to saliva

The computational analysis was based on a physicochemical model of hydroxyapatite (HAp) precipitation previously developed within the research group of Prof. Svetlana V. Komarova, where the present thesis work was conducted during the research stay at the University of Alberta [46, 42]. The model was originally formulated to describe aqueous ionic equilibria and HAp mineralization in interstitial fluid (ISF) within the bone microenvironment, and was subsequently incorporated into a broader framework integrating physicochemical and biological regulation of bone mineralization [51].

The physicochemical compartment describes an aqueous ionic system containing calcium, phosphate, carbonate, magnesium, sodium, chloride, and potassium as major components. Their total concentrations, together with the imposed pH, are used to calculate the equilibrium distribution of free and associated species, ionic strength, activity coefficients, and the saturation state of the solution with respect to HAp [42, 51].

In the present work, the equilibrium and saturation components of this physicochemical framework were adapted from bone interstitial fluid to a saliva-like ionic environment. The adaptation was based on the common mineralogical relevance of HAp in bone and dental enamel, while acknowledging that the two tissues and their surrounding fluids are biologically and chemically distinct. The model was therefore not used to reproduce bone-specific biological processes or precipitation kinetics, but rather as an aqueous equilibrium framework to investigate how salivary pH and ionic composition influence the thermodynamic saturation state of HAp under conditions relevant to the oral environment.

For the saliva-based analyses described in Sections 2.2.3–2.2.6, the original reaction network and equilibrium formulation were retained, apart from the coding correction described in Section 2.2.3, while the input composition was replaced by saliva-specific concentrations. These reported salivary concentrations were used as operational estimates of the total component inputs required by the model. The saliva adaptation therefore retained the seven-component chemical framework of the original model, while additional salivary constituents and macromolecular interactions were not explicitly represented.

The input vector was defined as

$$\mathbf{T} = [T_{CO_3}, T_{PO_4}, T_{Ca}, T_{Mg}, T_{Na}, T_{Cl}, T_K], \tag{2.1}$$

where T_{CO_3}, T_{PO_4}, T_{Ca}, T_{Mg}, T_{Na}, T_{Cl}, and T_K denote the total component concentrations used by the equilibrium model for carbonate, phosphate, calcium, magnesium, sodium, chloride, and potassium, respectively.

2.2.2 Equilibrium calculation, activity correction and HAp saturation

For each defined fluid composition, the model calculates the equilibrium distribution of the major ionic components among their free and associated chemical forms. The physicochemical system includes acid–base equilibria of the carbonate and phosphate systems, together with complexation reactions involving calcium, magnesium, sodium, and potassium [42, 51]. In the MATLAB implementation used in this work, the equilibrium formulation includes 22 reversible reactions describing the distribution of the seven major components among their free and associated chemical forms. Together with one equation defining pH and seven mass-conservation equations, these relationships form a system of 30 equations, which is subsequently reduced to seven nonlinear equations in seven variables.

The total concentration of each major component is conserved and distributed among its corresponding species. For example, total calcium includes free Ca^{2+} as well as calcium-containing complexes such as $CaHCO_3^+$, $CaCO_3(aq)$, $CaOH^+$, $CaH_2PO_4^+$, $CaHPO_4(aq)$, and $CaPO_4^-$. Similarly, total phosphate is distributed among its different protonation states and associated complexes. Using the equilibrium relationships, the complete system is reduced to a set of nonlinear mass-balance equations, which are solved numerically using the Newton–Raphson method [46, 42, 51].

Since the modeled fluid is an ionic solution, non-ideal interactions between charged species are taken into account through activity corrections. The ionic strength, I, is calculated as

$$I = \frac{1}{2} \sum_i c_i z_i^2, \tag{2.2}$$

where c_i represent the molar concentration of ion i and z_i is its valence respectively [46, 42].

Activity coefficients are subsequently calculated using the Davies equation:

$$\log_{10} \gamma_i = -A z_i^2 \left(\frac{\sqrt{I}}{1 + \sqrt{I}} - 0.3I \right), \tag{2.3}$$

where γ_i is the activity coefficient of species i. The temperature-dependent parameter A is calculated at 37 °C according to

$$A = 0.486 + 6.07 \times 10^{-4} T + 6.43 \times 10^{-6} T^2, \tag{2.4}$$

where T is expressed in degrees Celsius [46, 42]. In accordance with the original model, the Davies formulation was adopted consistently with the original physicochemical model [42]. Its stated applicability is limited to ionic strengths of approximately $I \leq 0.5\,\mathrm{M}$.

Equilibrium concentrations and activity coefficients are determined iteratively. Starting from initial estimates of the activity coefficients, the equilibrium concentrations and ionic strength are calculated, the activity coefficients are updated, and the procedure is repeated until convergence. In accordance with the original implementation, convergence was considered achieved when the maximum difference between two consecutive sets of activity coefficients was lower than 10^{-8} [46, 42].

The thermodynamic activity of each species was represented as

$$a_i = \gamma_i c_i, \tag{2.5}$$

where c_i and γ_i denote the equilibrium concentration and activity coefficient of species i, respectively.

Once equilibrium and activity corrections had converged, the saturation state of the solution with respect to hydroxyapatite was calculated. Consistently with the original physicochemical model, hydroxyapatite was represented using the reduced stoichiometric formula

$$\mathrm{Ca_5(PO_4)_3OH}. \tag{2.6}$$

The original model defines the ionic product (IP) as [42, 51]

$$IP = \left(c_{\mathrm{Ca^{2+}}}\gamma_{\mathrm{Ca^{2+}}}\right)^5 \left(c_{\mathrm{PO_4^{3-}}}\gamma_{\mathrm{PO_4^{3-}}}\right)^3 \left(c_{\mathrm{OH^-}}\gamma_{\mathrm{OH^-}}\right). \tag{2.7}$$

Since $a_i = \gamma_i c_i$, the same quantity can equivalently be expressed as the ion activity product (IAP),

$$IAP = a_{\mathrm{Ca^{2+}}}^5 a_{\mathrm{PO_4^{3-}}}^3 a_{\mathrm{OH^-}}. \tag{2.8}$$

Thus, the IAP notation used in the present work is mathematically equivalent to the IP definition adopted in the original physicochemical model.

A hydroxyapatite solubility product of

$$K_{sp} = 2.03 \times 10^{-59}\,\mathrm{mol^9\,L^{-9}} \tag{2.9}$$

at 37 °C was used, consistently with the original physicochemical model [42, 51]. The supersaturation ratio was then calculated as

$$S = \left(\frac{IAP}{K_{sp}}\right)^{1/9}, \tag{2.10}$$

where the exponent 1/9 corresponds to the reciprocal of the sum of the stoichiometric coefficients in the reduced HAp formula [42, 51].

Accordingly, $S < 1$ indicates undersaturation with respect to HAp, $S = 1$ represents thermodynamic equilibrium, and $S > 1$ indicates supersaturation. In the present work,

S was used exclusively as a thermodynamic descriptor of the saliva-like environment. In applying this framework to dental enamel, stoichiometric HAp was used as a simplified thermodynamic representation of the enamel mineral phase; compositional substitutions characteristic of biological enamel apatite and alternative calcium-phosphate mineral phases were not explicitly represented. Furthermore, undersaturation was not interpreted as a direct simulation of enamel dissolution, since dissolution kinetics were not included in the model.

2.2.3 Model verification and saliva baseline definition

Before applying the physicochemical framework to saliva, the MATLAB implementation was verified under the reference bone interstitial fluid conditions reported for the original model. The published physiological input composition was reproduced, and the calculated ionic strength and hydroxyapatite supersaturation ratio were compared with the corresponding reference values reported by Poorhemati and Komarova [42]. This verification step was performed to ensure that the equilibrium, activity-correction, and saturation calculations were correctly reproduced before adapting the model to a saliva-like environment.

During inspection of the MATLAB implementation, the equilibrium expression associated with the $NaH_2PO_4(aq)$ species was also reviewed. A formal inconsistency was identified in the variable used within the corresponding phosphate complexation term. A corrected implementation was therefore generated and compared with the original code under both the reference interstitial-fluid condition and the saliva baseline condition. The comparison included ionic strength (I), ionic activity product (IAP), hydroxyapatite supersaturation ratio, and the predicted saturation crossover pH. The corrected implementation was subsequently used for the saliva-based analyses.

As an additional semi-quantitative external comparison of the saliva-adapted framework, model predictions were compared with experimental data reported for stimulated human saliva before and after acidification [39]. Mean pH, total calcium, and total phosphate concentrations reported for the medium buffering-capacity group were used as model inputs under the initial condition and after titration with 50 μL HCl. Because the experimental study did not report the complete ionic composition required by the present model, the remaining ionic components were maintained at the reference saliva values. The comparison was based on the change in $\log_{10}$ hydroxyapatite ionic activity product(IAP) between the initial and acidified conditions and was used as a qualitative and semi-quantitative assessment of whether the adapted model reproduced the experimentally observed decrease in HAp ion activity product with acidification.

For the saliva-adapted model, a reference composition was defined from the mean concentrations reported for **unstimulated whole human saliva** [38]. The values used were:

$$\mathrm{pH} = 7.04 \tag{2.11}$$

$$T_{\mathrm{CO_3}} = 5.47\,\mathrm{mM} \tag{2.12}$$

$$T_{PO_4} = 5.69\,\text{mM} \tag{2.13}$$

$$T_{Ca} = 1.32\,\text{mM} \tag{2.14}$$

$$T_{Mg} = 0.20\,\text{mM} \tag{2.15}$$

$$T_{Na} = 5.76\,\text{mM} \tag{2.16}$$

$$T_{Cl} = 16.40\,\text{mM} \tag{2.17}$$

$$T_{K} = 19.47\,\text{mM}. \tag{2.18}$$

These values correspond to the mean inorganic composition of unstimulated whole saliva summarized by Uchida and Ovitt, including sodium, potassium, calcium, magnesium, chloride, bicarbonate, and phosphate concentrations [38].

Because the original physicochemical model requires total component concentrations, the reported ionic concentrations were used as operational estimates of the corresponding total component inputs. In particular, the reported bicarbonate concentration was used as an approximation of the total carbonate component, T_{CO_3}, while the reported calcium and phosphate concentrations were used as estimates of T_{Ca} and T_{PO_4}, respectively. These assumptions were maintained consistently throughout the saliva-based simulations.

The resulting reference composition was used as the baseline condition for the subsequent pH-dependent, sensitivity, literature-based saliva scenario, calcium–phosphate interaction, and multidimensional uncertainty analyses. Alternative ionic compositions were introduced only in the dedicated simulations described in the following sections.

2.2.4 pH-dependent saturation and sensitivity analyses

The effect of pH on the hydroxyapatite saturation state of the reference saliva composition was investigated by performing a systematic pH sweep. The input pH was varied from 3.0 to 8.0 in increments of 0.05, while all total component concentrations were kept fixed at the baseline values defined in Section 2.2.3. For each pH value, equilibrium speciation, ionic strength, activity coefficients, ionic activity product, and the hydroxyapatite supersaturation ratio S were recalculated using the corrected physicochemical model [42].

The pH corresponding to the transition between undersaturation and supersaturation was identified from the condition

$$S = 1. \tag{2.19}$$

This value was defined as the predicted hydroxyapatite saturation crossover pH, $pH_{S=1}$. The crossover was determined numerically by interpolation between adjacent pH values for which the calculated supersaturation ratio changed from below to above unity. In

the present work, $pH_{S=1}$ was used as a model-derived descriptor of the thermodynamic saturation transition and was not interpreted as a universal critical pH for dental enamel. The strong dependence of the hydroxyapatite ion activity product on pH and phosphate speciation has also been described experimentally in saliva-related systems [39].

To assess the influence of individual salivary components on the predicted crossover, one-at-a-time sensitivity analyses were performed. Calcium, phosphate, and carbonate concentrations were initially varied between 50% and 150% of the reference values, while all other components were kept fixed. For each modified composition, the complete pH sweep was repeated and the corresponding $pH_{S=1}$ was calculated. This first analysis was used to compare the relative influence of the main mineral-related components on the predicted hydroxyapatite saturation transition.

To further examine the chemical basis of the first one-at-a-time sensitivity analysis, equilibrium concentrations of selected species were evaluated at the reference input pH while calcium, phosphate, or carbonate concentrations were varied between 50% and 150% of their baseline values. Particular attention was given to free Ca^{2+}, $H_2PO_4^-$, HPO_4^{2-}, PO_4^{3-}, and $CaHPO_4(aq)$, since calcium and phosphate speciation directly influence the hydroxyapatite ionic activity product [42, 39].

A second sensitivity analysis was performed over selected literature-informed working ranges. The investigated intervals were selected to be consistent with concentration domains reported for human saliva across different studies, rather than to represent fixed physiological limits [38, 39, 35, 36]. The selected ranges were 0.95–2.15 mM for calcium and 4.00–6.00 mM for phosphate. Additional exploratory ranges of 0.10–0.37 mM for magnesium, 1.72–10.32 mM for sodium, 14.87–23.21 mM for potassium, and 9.31–26.95 mM for chloride were considered.

All sensitivity analyses were interpreted within the concentration intervals investigated. Because different ions were explored over different absolute or relative ranges, the resulting changes in $pH_{S=1}$ were used to describe model sensitivity under the selected conditions rather than to define universal sensitivity coefficients.

2.2.5 Literature-based saliva scenarios and Ca–PO_4 interaction analysis

To investigate differences in saliva composition reported in the literature, additional simulations were performed using alternative saliva states derived from published data. In particular, unstimulated and mastication-stimulated whole saliva conditions were defined using experimentally reported values of pH, bicarbonate, sodium, potassium, and chloride [33]. Because calcium, phosphate, and magnesium concentrations were not reported in that dataset, these components were maintained at the reference baseline values defined in Section 2.2.3. As in the baseline simulations, the reported bicarbonate concentration was used as an approximation of the model input T_{CO_3}.

For each literature-based saliva scenario, the equilibrium calculation was repeated using the same physicochemical model and activity-correction procedure described above. The resulting thermodynamic state was characterized in terms of ionic strength, ionic activity product, hydroxyapatite supersaturation ratio, and the predicted saturation crossover

pH, $pH_{S=1}$. In addition, selected equilibrium species were examined in order to assess how stimulation-related changes in pH and electrolyte composition affected calcium and phosphate speciation.

Because calcium and phosphate are directly involved in hydroxyapatite saturation, their combined effect was further investigated through two-dimensional interaction analyses. Calcium and phosphate were varied simultaneously over the working ranges 0.95–2.15 mM and 4.00–6.00 mM, respectively, while all remaining components were kept fixed at the reference saliva composition [38, 35]. For each calcium–phosphate combination, the model was solved and the corresponding supersaturation ratio S was calculated.

The interaction maps were evaluated at pH 5.00, 5.15, and 5.50, representing conditions below, near, and above the reference saturation crossover, respectively. The resulting two-dimensional maps were used to visualize regions of undersaturation, near-equilibrium, and supersaturation with respect to hydroxyapatite. For the quantitative classification of the explored Ca–PO_4 domain, $S < 0.99$ was considered undersaturated, $0.99 \leq S \leq 1.01$ near equilibrium, and $S > 1.01$ supersaturated. These regions were used only as descriptors of the explored parameter space and were not interpreted as probabilities of physiological occurrence.

The combined calcium–phosphate analysis was intended to complement the one-at-a-time sensitivity analysis described in Section 2.2.4 by examining whether simultaneous variation of the two principal mineral-related components altered the predicted thermodynamic state of the saliva-like solution.

2.2.6 Exploratory multidimensional uncertainty analysis

To evaluate the robustness of the predicted hydroxyapatite saturation crossover to simultaneous variation in multiple salivary components, an exploratory multidimensional uncertainty analysis was performed. Calcium, phosphate, magnesium, sodium, potassium, and chloride concentrations were varied simultaneously within the literature-informed working ranges introduced in Section 2.2.4, while carbonate was varied between 50% and 150% of its reference value.

A total of 500 parameter combinations were generated by independently sampling each ionic component from a uniform distribution over its assigned working interval. The investigated intervals were 0.95–2.15 mM for calcium, 4.00–6.00 mM for phosphate, 2.735–8.205 mM for carbonate, 0.10–0.37 mM for magnesium, 1.72–10.32 mM for sodium, 14.87–23.21 mM for potassium, and 9.31–26.95 mM for chloride [38, 36, 35].

For each sampled composition, the presence of an $S = 1$ crossing within pH 4.0–6.2 was evaluated, and the corresponding $pH_{S=1}$ was determined by numerical bisection when a valid sign change was present. The resulting distribution of $pH_{S=1}$ values was summarized using descriptive statistics, including the mean, standard deviation, median, range, and selected percentiles.

To explore the association between individual input variables and variability in the predicted crossover pH, Pearson correlation coefficients were calculated between each sampled ionic concentration and the corresponding $pH_{S=1}$. These correlations were used as exploratory indicators of the direction and strength of linear associations within the selected

multidimensional parameter space, rather than as formal measures of causal contribution or global sensitivity.

Because the input values were sampled independently from uniform distributions and were not intended to reproduce the statistical distribution or correlation structure of salivary composition in a real population, the analysis was interpreted as a model robustness and uncertainty assessment rather than as a physiological population simulation.

An additional exploratory acidification stress test, based on a plaque-derived pH trajectory applied to the reference saliva composition, is reported in Appendix A.

2.2.7 Thermodynamic characterization of the experimental treatment solutions

To establish a direct link between the experimental treatment protocol and the computational framework, the equilibrium model was further applied to characterize the thermodynamic conditions generated by the treatment solutions used for enamel exposure. The experimentally prepared mineral solution contained KCl, NaCl, $CaCl_2{\cdot}2H_2O$, Na_2HPO_4, and $NaHCO_3$, as described in Section 2.1.3. Using 160 mL as the nominal reference volume, the experimental recipe was converted into total model-component concentrations of 209.587 mM K, 90.070 mM Na, 273.507 mM Cl, 2.551 mM Ca, 6.252 mM phosphate, and 18.749 mM carbonate. Magnesium was set to zero because it was not included in the experimental formulation. Changes in final volume associated with subsequent acid and base additions were neglected, and thymol and ethanol used for preservation were not included in the equilibrium calculations.

The remineralization solution was represented using the experimentally imposed pH of 7.0 and no lactate. The demineralization solution was represented at the experimentally imposed pH of 4.0 with a total lactic acid/lactate concentration of 100 mM. Because lactate chemistry was not included in the original equilibrium framework, the model was extended by introducing the acid dissociation equilibrium.

$$\mathrm{HLac} \rightleftharpoons \mathrm{H^+} + \mathrm{Lac^-}, \tag{2.20}$$

together with formation of the 1:1 calcium–lactate complex

$$\mathrm{Ca^{2+}} + \mathrm{Lac^-} \rightleftharpoons \mathrm{CaLac^+}. \tag{2.21}$$

For the purpose of this exploratory analysis, lactic acid dissociation was represented using a pK_a value of 3.86, consistent with literature data reported for lactic acid [52]. Since this value was not independently determined under the specific temperature and ionic-strength conditions represented in the present model, it was treated as a modelling assumption rather than as an experimentally validated parameter for the treatment solution.

The corresponding lactate mass balance was added to the nonlinear equilibrium system, and $CaLac^+$ was included simultaneously in the calcium mass balance, ionic-strength calculation, and activity correction. Hydroxyapatite saturation was then calculated using the same activity-based ion activity product and supersaturation definition described in Section 2.2.2.

A calcium–lactate association constant of approximately 8 L/mol has been experimentally reported for 1:1 Ca–lactate complex formation under defined solution conditions [53]. This value was therefore selected as a literature-based reference condition for the present exploratory extension of the model. However, because the reported association constant was determined under conditions different from those of the present system, and no Ca–lactate association constant was experimentally determined for the treatment solution used in this study, it was not regarded as an independently validated parameter for the present model.

To evaluate the sensitivity of the predicted HAp saturation state to the assumed strength of Ca–lactate association, additional association constants were considered:

$$K_{\mathrm{CaLac}} = 3,\ 8,\ \text{and } 20\,\mathrm{L/mol}. \tag{2.22}$$

The values of 3 and 20 L/mol were introduced as lower and upper exploratory cases, respectively, and were not intended to represent experimentally validated equilibrium constants for the treatment solution. The literature-supported value of $K_{\mathrm{CaLac}} = 8\,\mathrm{L/mol}$ was retained as the representative condition for the main comparison.

An additional case with $K_{\mathrm{CaLac}} = 0$ was introduced as a mechanistic computational reference in which lactate remained present in the solution but formation of $CaLac^{+}$ was disabled. A separate pH 4 condition without lactate was also evaluated to distinguish the effect of acidification alone from the effects associated with lactate-containing chemistry.

The experimental demineralization solution had been adjusted to pH 4 using NaOH, but the exact amount of titrant added during preparation was not available. Consequently, the sodium contribution associated with pH adjustment could not be reconstructed directly from the experimental recipe. For each lactate-containing simulation, the additional total Na concentration was therefore estimated computationally by imposing electroneutrality,

$$\sum_i z_i c_i = 0, \tag{2.23}$$

where z_i and c_i are the charge and equilibrium concentration of species i, respectively. The additional Na concentration was varied iteratively using a bisection procedure until the absolute charge-balance residual was below 1×10^{-8} M.

The electroneutrality-based sodium correction was applied only to the lactate-containing simulations; the nominal remineralization solution and the pH 4 no-lactate reference condition were retained without additional sodium correction. This correction was introduced only to obtain an electrically consistent representation of the modelled solution and was not interpreted as an exact reconstruction of the experimentally added NaOH amount.

For each condition, the model returned the equilibrium ionic strength, free Ca^{2+}, free PO_4^{3-}, $CaLac^{+}$, lactate speciation, ion activity product, and HAp supersaturation ratio S. Calcium partitioning was additionally expressed as the fraction of total calcium present as free Ca^{2+}, $CaLac^{+}$, or other Ca-containing aqueous species.

Chapter 3

Results

3.1 Experimental Results

3.1.1 Baseline Raman characterization

Baseline Raman spectra of the untreated bovine enamel specimens BT0 and BT1 are shown in Figure 3.1. Both specimens exhibited the characteristic spectral profile of enamel apatite. The dominant band was observed at approximately **960 cm^{-1}** and was assigned to the ν_1 symmetric stretching mode of PO_4^{3-}. Additional phosphate-related bands were identified at approximately **430 cm^{-1}** (ν_2), **580 cm^{-1}** (ν_4), and in the region around **1040 cm^{-1}** (ν_3). A carbonate-associated contribution was also observed around **1070 cm^{-1}**, corresponding to the ν_1 vibrational mode of CO_3^{2-}.

The spectra obtained from BT0 and BT1 showed a similar overall spectral profile, with the main phosphate- and carbonate-related bands occurring at comparable Raman shifts. In both untreated specimens, the intense and well-defined ν_1 phosphate band at approximately 960 cm^{-1} represented the predominant spectral feature. The spectra of BT0 and BT1 were therefore used as the **baseline Raman characterization of untreated bovine enamel** for comparison with the subsequently treated specimens.

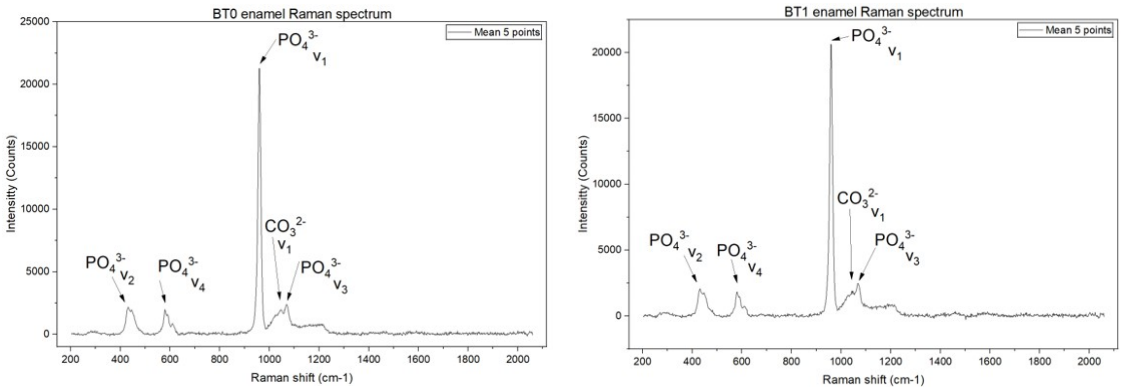


Figure 3.1: Baseline Raman spectra of untreated bovine enamel specimens BT0 and BT1. Each spectrum represents the mean of measurements acquired at five different points across the enamel surface. The main phosphate-related bands and the carbonate-associated band are indicated.

3.1.2 Baseline SEM/EDS characterization

SEM imaging of the untreated reference enamel revealed a densely packed surface morphology at high magnification. At approximately 90,000× and 100,000×, the enamel surface showed irregular nanoscale mineral features separated by visible boundaries, with a generally compact and heterogeneous organization.

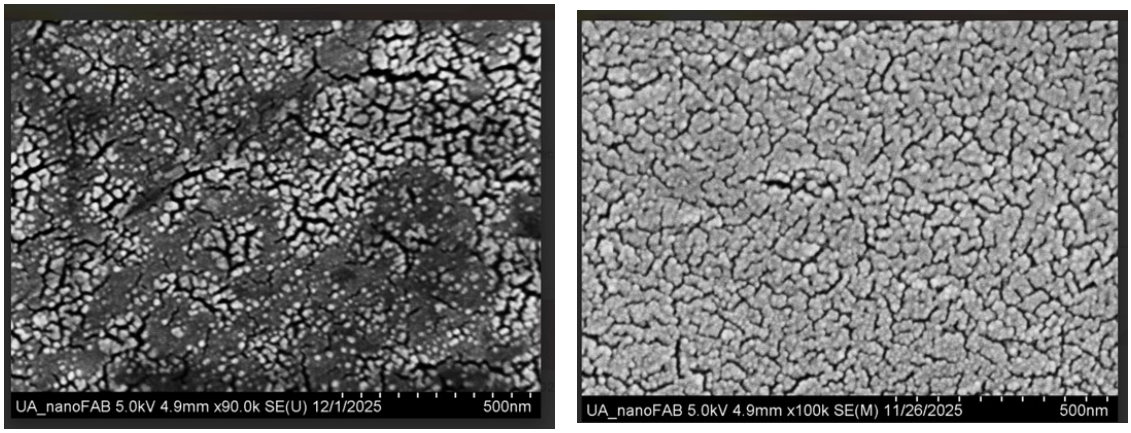


Figure 3.2: Baseline SEM characterization of untreated bovine enamel. Representative high-magnification SEM images acquired at approximately (a) 90,000× and (b) 100,000×, showing the nanoscale surface morphology of the enamel.

EDS analysis of the untreated enamel showed prominent signals corresponding to phosphorus (P), calcium (Ca), and oxygen (O). Lower-intensity signals associated with carbon (C), magnesium (Mg), and sodium (Na) were also detected. The corresponding layered elemental map showed that the detected elements were distributed across the analyzed enamel region.

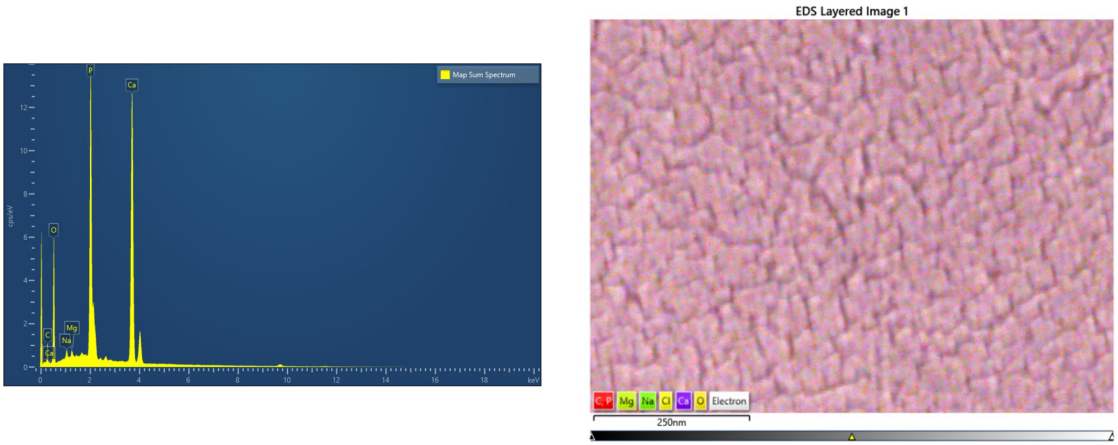


Figure 3.3: Baseline EDS characterization of untreated bovine enamel. (a) EDS spectrum of the analyzed enamel region, showing prominent signals associated with phosphorus, calcium, and oxygen, together with lower-intensity signals from other detected elements; (b) corresponding layered elemental map showing the spatial distribution of the detected elements across the analyzed region.

3.1.3 Baseline microhardness characterization

Vickers microhardness measurements were performed as part of the baseline mechanical characterization of the untreated enamel. Three indentations were analyzed, yielding hardness values of **39.8, 41.1, and 44.1 HV0.1** (Table 3.1). The corresponding indentation diagonals ranged from **63.54 to 68.23 μm**. The mean baseline microhardness was 41.7 ± 2.2 **HV0.1** (mean $\pm$ SD, $n = 3$).

Table 3.1: Baseline Vickers microhardness measurements of untreated bovine enamel. D1 and D2 represent the two diagonals of the residual Vickers indentation.

Measurement	**D1 (μm)**	**D2 (μm)**	**Hardness (HV0.1)**
1	68.23	68.23	39.8
2	66.71	67.62	41.1
3	63.54	66.14	44.1
Mean $\pm$ SD	–	–	41.7 ± 2.2

3.1.4 Raman characterization after the experimental treatments

Raman spectra acquired from BT5 after the 6-day experimental conditions retained the characteristic spectral features of enamel apatite. Under all experimental conditions, the dominant band was located at approximately **960 cm^{-1}**, corresponding to the ν_1 symmetric stretching vibration of PO_4^{3-}, together with additional phosphate-related bands at approximately **430 cm^{-1}** and **580 cm^{-1}**, as well as spectral contributions in the **1040–1070 cm^{-1}** region.

The spectra obtained under the **Demin condition** showed very similar profiles, with substantially overlapping band positions and comparable spectral shapes (Figure 3.4). A

similar agreement was observed between the spectra acquired under the **Remin condition** (Figure 3.5).

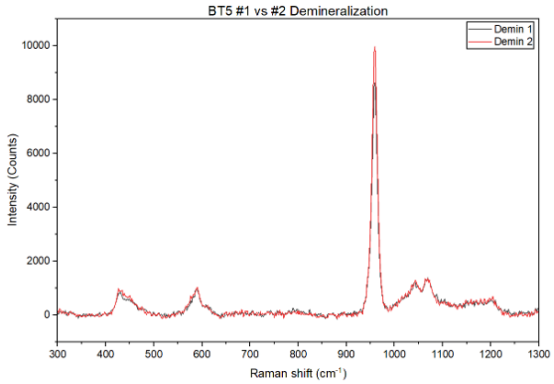


Figure 3.4: Comparison of Raman spectra acquired from BT5 under the Demin condition. Demin #1 and Demin #2 showed comparable spectral profiles and similar positions of the characteristic enamel apatite bands.

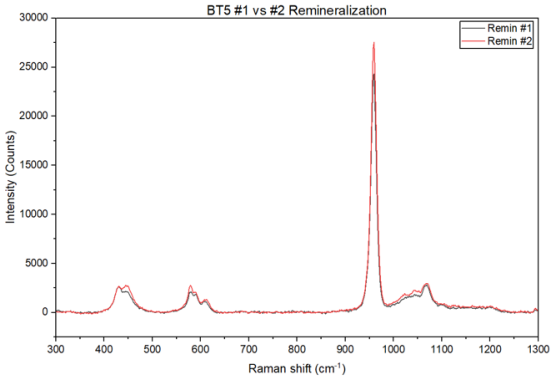


Figure 3.5: Comparison of Raman spectra acquired from BT5 under the Remin condition. Remin #1 and Remin #2 showed comparable spectral profiles and similar positions of the characteristic enamel apatite bands.

When the three experimental conditions were compared directly, the positions of the main Raman bands remained essentially unchanged, whereas differences in absolute signal intensity were observed. In the comparison between **Demin #1, Remin #1, and Dry #1** (Figure 3.6), the Demin spectrum showed the lowest intensity of the dominant phosphate band at approximately 960 cm^{-1}, while the Remin and Dry spectra exhibited higher intensities.

The same overall trend was observed in the second comparison using **Demin #2, Remin #2, and Dry #1** (Figure 3.7). Despite the observed differences in absolute signal intensity, the characteristic Raman fingerprint of enamel apatite remained detectable under all three experimental conditions.

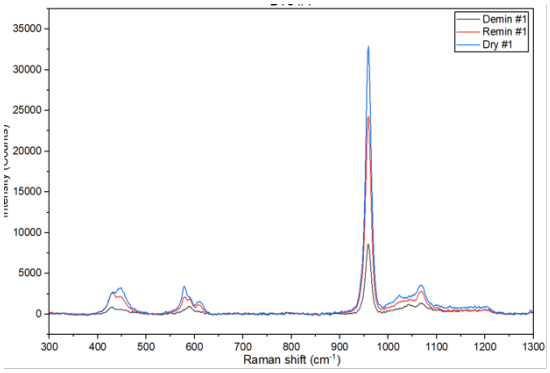


Figure 3.6: Comparison of Raman spectra acquired from BT5 under Demin #1, Remin #1, and Dry #1 conditions. Differences in absolute signal intensity were observed, while the characteristic Raman bands of enamel apatite remained detectable in all conditions.

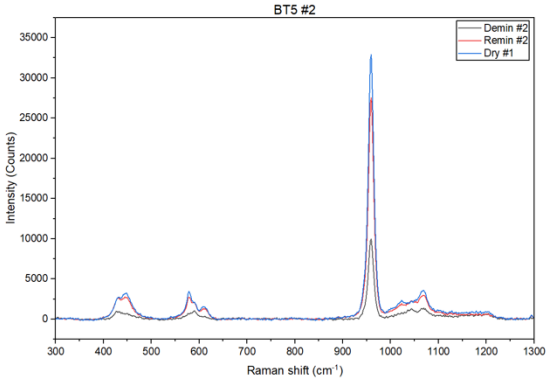


Figure 3.7: Comparison of Raman spectra acquired from BT5 under Demin #2, Remin #2, and Dry #1 conditions. The main Raman band positions remained comparable despite differences in absolute signal intensity.

3.1.5 SEM characterization after the experimental treatments

SEM imaging performed after the 6-day experimental period revealed differences in the surface morphology of BT5 specimens among the Demin, Remin, and Dry conditions. At the larger observation scales, all specimens displayed a heterogeneous enamel surface, while progressively higher magnification revealed differences in the organization of the surface features.

Under the **Demin condition** (Figure 3.8), the higher-magnification images showed a densely structured surface characterized by numerous irregular and elongated features, locally arranged in compact aggregates. These structures became particularly evident at the 1 μm scale.

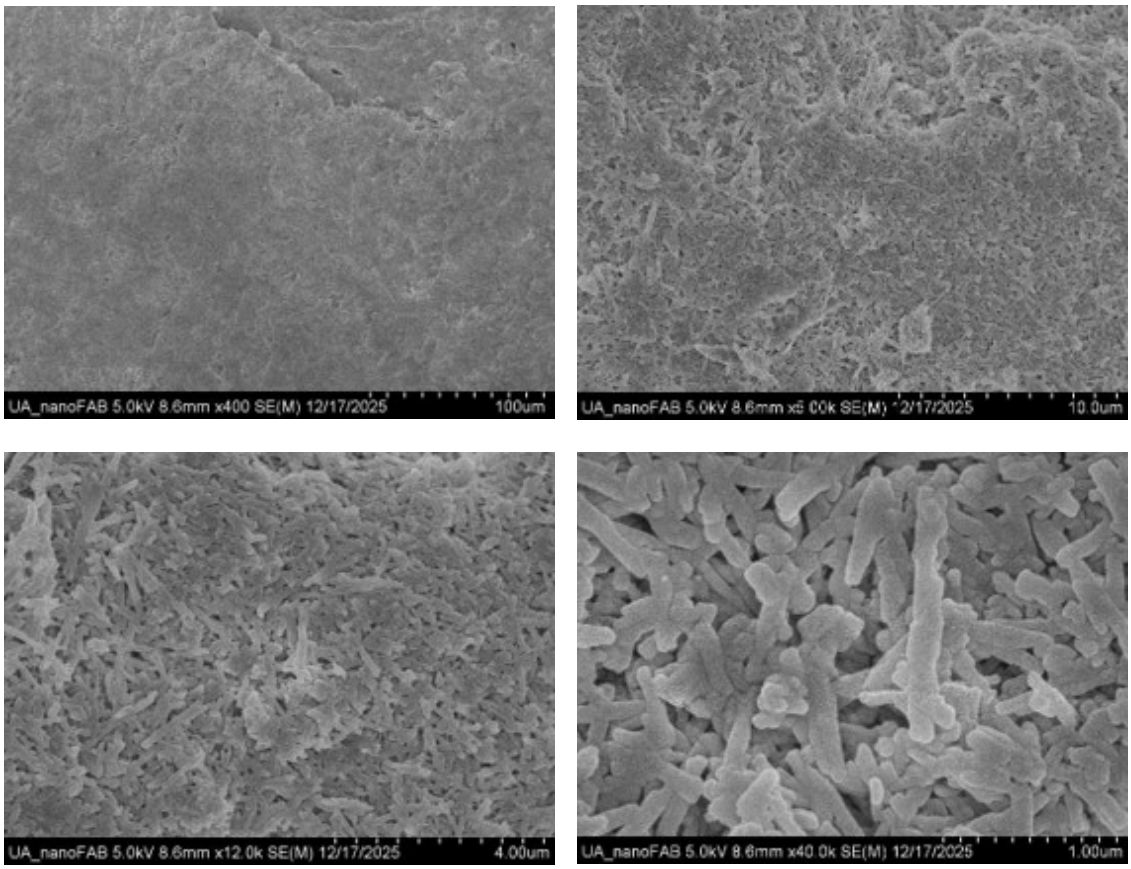


Figure 3.8: SEM characterization of BT5 after the Demin condition. Representative SEM images acquired after 6 days of exposure to the pH 4.0 demineralization solution, shown at progressively higher magnification with 100, 10, 4, and 1 μm scales.

The **Remin condition** (Figure 3.9) also exhibited elongated surface structures at high magnification. Compared with the Demin condition, these features appeared more individually distinguishable and distributed over a heterogeneous underlying surface, particularly in the 1 and 4 μm images.

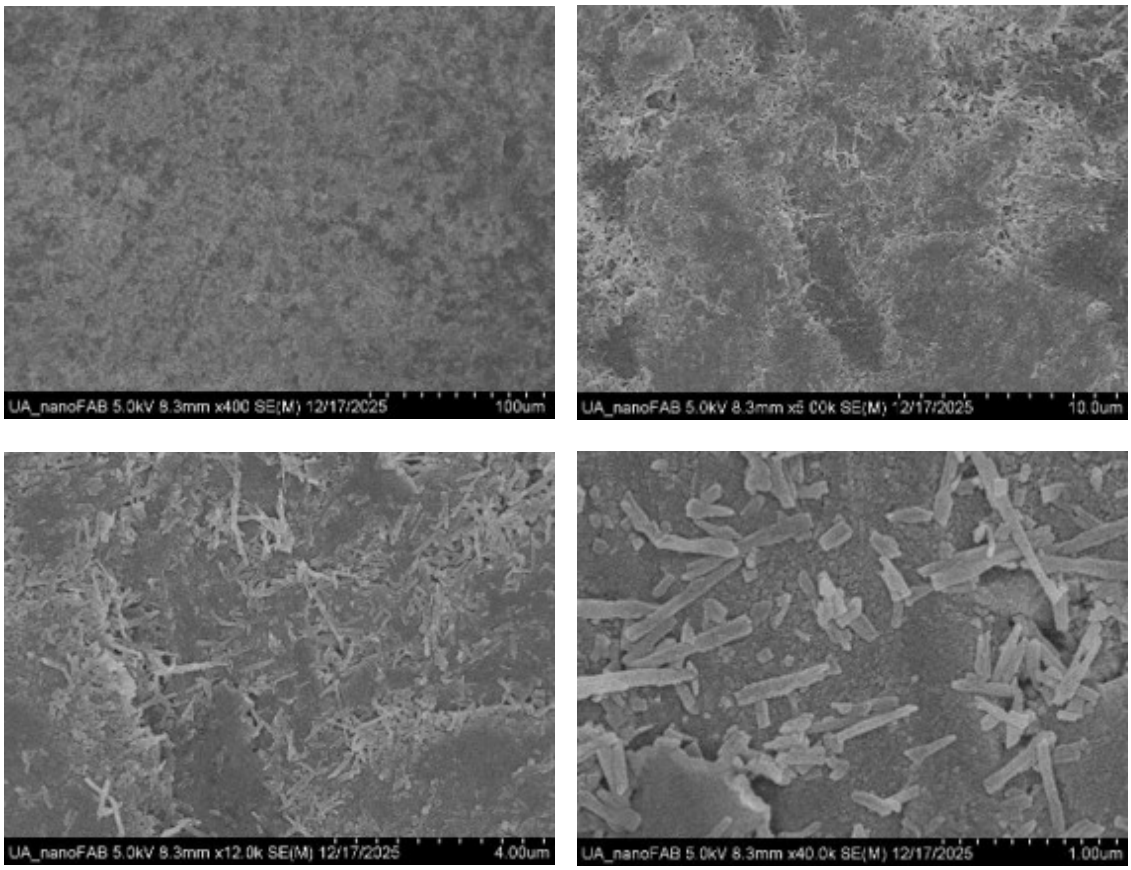


Figure 3.9: SEM characterization of BT5 after the Remin condition. Representative SEM images acquired after 6 days of exposure to the pH 7.0 mineral solution, shown at progressively higher magnification with 100, 10, 4, and 1 μm scales.

The **Dry control condition** (Figure 3.10) showed a heterogeneous surface morphology across the investigated scales. At high magnification, irregular surface aggregates together with less prominent elongated structures were visible. Overall, the three experimental conditions exhibited visually different patterns of nanoscale surface organization. No quantitative morphometric analysis of the SEM images was performed.

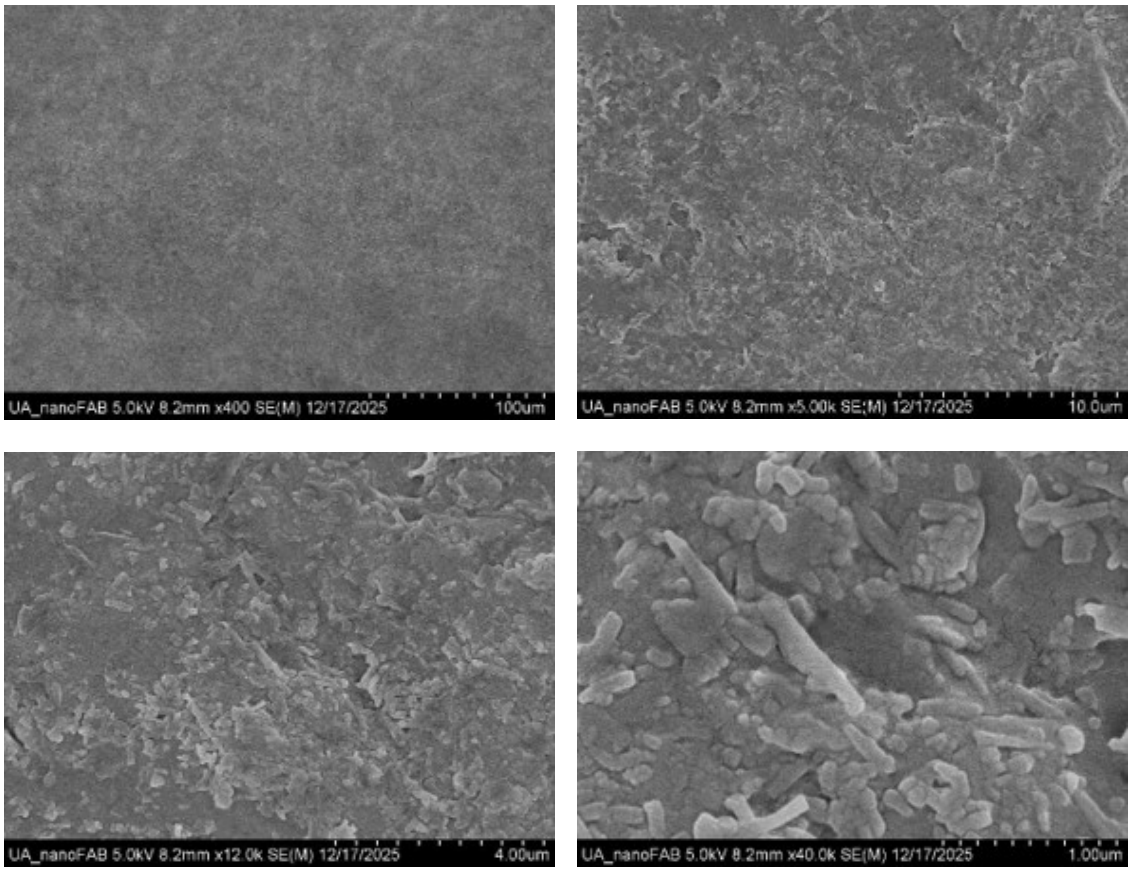


Figure 3.10: SEM characterization of BT5 under the Dry control condition. Representative SEM images of the specimen maintained for 6 days without solution exposure, shown at progressively higher magnification with 100, 10, 4, and 1 μm scales.

3.2 Computational Results

The computational analyses were performed using the saliva-adapted physicochemical framework described in Section 2.2. The results are presented starting from model verification and baseline characterization, followed by pH-dependent and sensitivity analyses, literature-based saliva scenarios, calcium–phosphate interaction analysis, multidimensional uncertainty assessment, and thermodynamic characterization of the experimental treatment solutions.

3.2.1 Model verification and saliva baseline

The MATLAB implementation closely reproduced the reference interstitial fluid (ISF) condition of the original physicochemical model [42]. The calculated ionic strength was 0.144478 M and the hydroxyapatite saturation ratio was $S = 14.9308$, compared with reference values of approximately 0.145 M and 14.9, respectively (Table 3.2). Comparison between the original and corrected implementations resulted in negligible changes in the calculated ionic strength, saturation ratio, and saturation crossover pH.

External comparison with experimental stimulated-saliva data [39] showed a marked decrease in hydroxyapatite saturation following acidification. The predicted saturation ratio decreased from $S = 22.9433$ under the initial condition to $S = 0.5832$ after acidification. The corresponding model-predicted ionic activity product (IAP) decreased by 14.3538 logarithmic units, compared with a decrease of 15.0835 logarithmic units in the experimentally reported IpHA, resulting in a difference of approximately 0.73 logarithmic units in the magnitude of the change (Table 3.3).

For the reference unstimulated whole-saliva composition [38], an input pH of 7.04 resulted in a calculated pH of 7.1141, an ionic strength of 0.032658 M, and a hydroxyapatite saturation ratio of $S = 17.5016$. The reference saliva condition was therefore supersaturated with respect to hydroxyapatite and was used as the baseline condition for the subsequent analyses.

Table 3.2: Comparison of the ionic strength and hydroxyapatite saturation ratio obtained with the present MATLAB implementation with the corresponding reference values reported by Poorhemati and Komarova [42].

Parameter	**Reference model**	**Present MATLAB implementation**
Ionic strength, I (M)	~ 0.145	0.144478
HAp saturation ratio, S	~ 14.9	14.9308

Table 3.3: Comparison between experimentally reported hydroxyapatite ionic activity product (IpHA) in stimulated human saliva and the corresponding model predictions before and after acidification. Experimental values were obtained from [39].

Condition	**Experimental pH**	**Activity-corrected pH**	**Experimental IpHA**	**Model-predicted IAP**	**Model-predicted S**
Initial	7.40	7.4724	1.2×10^{-44}	3.5778×10^{-47}	22.9433
Acidified	5.00	5.0694	9.9×10^{-60}	1.5842×10^{-61}	0.5832

3.2.2 pH-dependent saturation and sensitivity analysis

Hydroxyapatite saturation showed a pronounced dependence on pH under the reference saliva composition. Across the investigated pH range from 3.00 to 8.00, the saturation ratio increased from $S = 0.0209$ to $S = 44.7881$, with an estimated saturation crossover at $pH_{S=1} = 5.1508$ (Figure 3.11). The model therefore predicted undersaturation with respect to hydroxyapatite below the crossover and saturation above it.

The pH-dependent variation was accompanied by marked changes in phosphate speciation (Figure 3.12). In particular, PO_4^{3-} increased by several orders of magnitude across the investigated pH range, together with a progressive shift in the relative contributions of $H_2PO_4^-$ and HPO_4^{2-}.

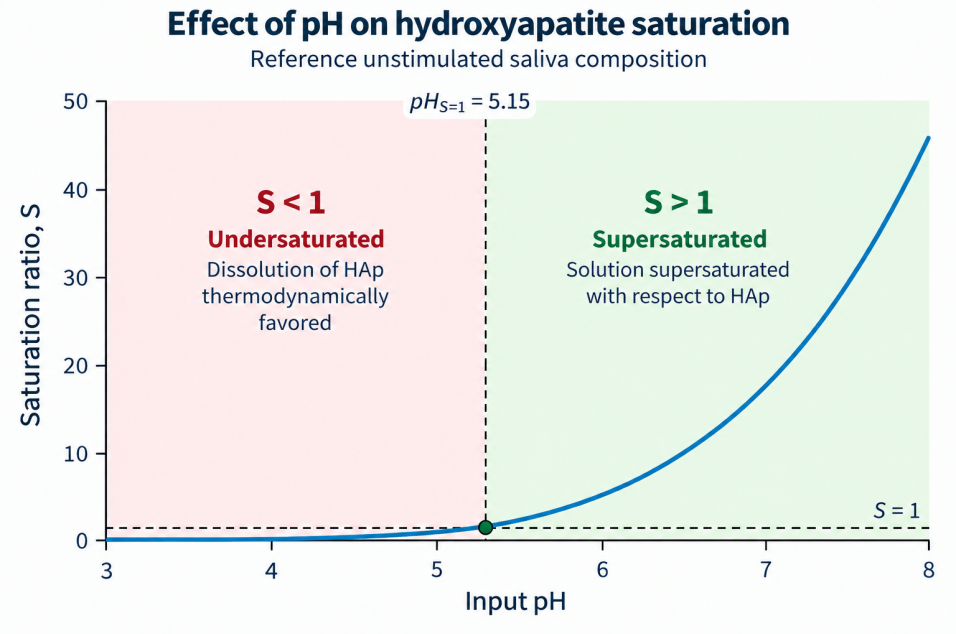


Figure 3.11: Hydroxyapatite saturation ratio as a function of pH for the reference saliva composition [38]

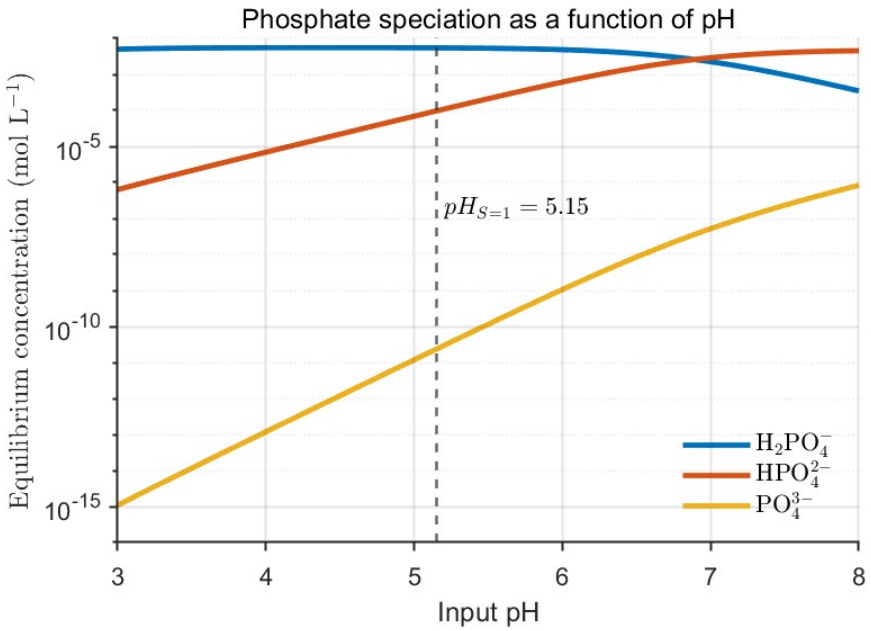


Figure 3.12: Phosphate speciation as a function of pH for the reference saliva composition.

The one-at-a-time sensitivity analysis showed different effects of calcium, phosphate, and carbonate on the predicted saturation crossover. When each component was varied from 50% to 150% of its reference concentration, the crossover range was 0.3406 pH units for calcium, 0.1735 pH units for phosphate, and 0.0160 pH units for carbonate. Increasing calcium and phosphate progressively shifted $pH_{S=1}$ toward lower values, whereas increasing carbonate produced only a small shift toward higher values.

Examination of equilibrium speciation at the reference input pH showed that the effects of calcium and phosphate variation were accompanied by changes in the distribution of HAp-related species. Increasing total calcium increased free Ca^{2+} and $CaHPO_4$(aq), while slightly decreasing the concentrations of the free phosphate species. Conversely, increasing total phosphate increased the concentrations of the phosphate species and $CaHPO_4$(aq), while decreasing free Ca^{2+}. Variation in total carbonate produced comparatively smaller changes in the selected calcium–phosphate species. These speciation changes were consistent with the stronger sensitivity of the predicted HAp saturation state to calcium and phosphate than to carbonate.

Sensitivity was subsequently evaluated over the literature-informed working ranges defined in Section 2.2.4. Calcium produced the largest variation in the crossover, with $pH_{S=1}$ decreasing from 5.2528 at 0.95 mM to 5.0017 at 2.15 mM, corresponding to a range of 0.2511 pH units. For phosphate, the crossover decreased from 5.2069 at 4.00 mM to 5.1424 at 6.00 mM, corresponding to a range of 0.0645 pH units. Within the investigated working ranges, magnesium, sodium, potassium, and chloride produced smaller variations in the predicted crossover, with ranges of 0.0010, 0.0079, 0.0078, and 0.0160 pH units, respectively (Table 3.4).

Table 3.4: Predicted variation in the hydroxyapatite saturation crossover over the literature-informed working ranges considered for the salivary ionic components.

Component	Investigated range (mM)	$pH_{S=1}$ at lower limit	$pH_{S=1}$ at upper limit	Crossover range (pH units)
Calcium	0.95–2.15	5.2528	5.0017	**0.2511**
Phosphate	4.00–6.00	5.2069	5.1424	**0.0645**
Chloride	9.31–26.95	5.1437	5.1597	**0.0160**
Sodium	1.72–10.32	5.1469	5.1548	**0.0079**
Potassium	14.87–23.21	5.1463	5.1541	**0.0078**
Magnesium	0.10–0.37	5.1504	5.1514	**0.0010**

3.2.3 Literature-based unstimulated and stimulated saliva scenarios

The unstimulated and stimulated saliva scenarios showed distinct hydroxyapatite saturation conditions (Table 3.5). At their respective input pH values, the saturation ratio increased from $S = 13.3029$ in unstimulated saliva to $S = 24.8981$ in stimulated saliva. This increase was accompanied by a higher ionic strength, from 0.031133 M to 0.048817 M, and by an increase in the ionic activity product from 2.6489×10^{-49} to 7.4688×10^{-47}, corresponding to a change of 2.4502 log units.

Despite the marked difference in saturation at the respective input pH values, the predicted saturation crossover showed only a limited shift, increasing from $pH_{S=1} = 5.1528$ in the unstimulated condition to 5.2132 in the stimulated condition, corresponding to a difference of 0.0604 pH units.

The two conditions also showed differences in the distribution of HAp-related ionic species. From the unstimulated to the stimulated condition, PO_4^{3-} increased approximately 9.16-fold and OH^- 4.64-fold, whereas free Ca^{2+} decreased by 19.3%. The concentration of $CaHPO_4$(aq) showed a smaller increase of 10.4%.

Table 3.5: Main physicochemical and hydroxyapatite saturation outputs predicted for the unstimulated and stimulated saliva scenarios.

Parameter	Unstimulated saliva	Stimulated saliva
Input pH	6.81	7.45
HCO_3^- (mM)	7.2	28.5
Ionic strength (M)	0.031133	0.048817
IAP	2.6489×10^{-49}	7.4688×10^{-47}
Saturation ratio, S	13.3029	24.8981
pH at $S = 1$	5.1528	5.2132

3.2.4 Calcium–phosphate interaction maps

The combined influence of calcium and phosphate on hydroxyapatite saturation was evaluated within the investigated concentration ranges of 0.95–2.15 mM for total calcium and 4.00–6.00 mM for total phosphate. At pH 5.15, close to the saturation crossover identified for the reference saliva composition, the baseline condition ($T_{Ca} = 1.32$ mM and $T_{PO_4} = 5.69$ mM) yielded $S = 0.9985$. Across the investigated calcium–phosphate domain, S ranged from 0.7564 to 1.3175, encompassing both undersaturated and supersaturated

conditions (Figure 3.13). The $S = 1$ boundary shifted toward higher calcium concentrations as total phosphate decreased, defining the combinations of the two components associated with the transition between the two saturation states.

The distribution of saturation states across the same calcium–phosphate domain changed markedly with pH (Figure 3.14). At pH 5.00, the baseline saturation ratio was 0.7666, and 99.04% of the investigated domain was classified as undersaturated, 0.94% as near equilibrium, and 0.02% as supersaturated. At pH 5.15, the corresponding fractions were 37.32%, 4.33%, and 58.35%, respectively, with a baseline S of 0.9985. At pH 5.50, the baseline saturation ratio increased to 1.8359 and the entire investigated domain (100%) was classified as supersaturated.

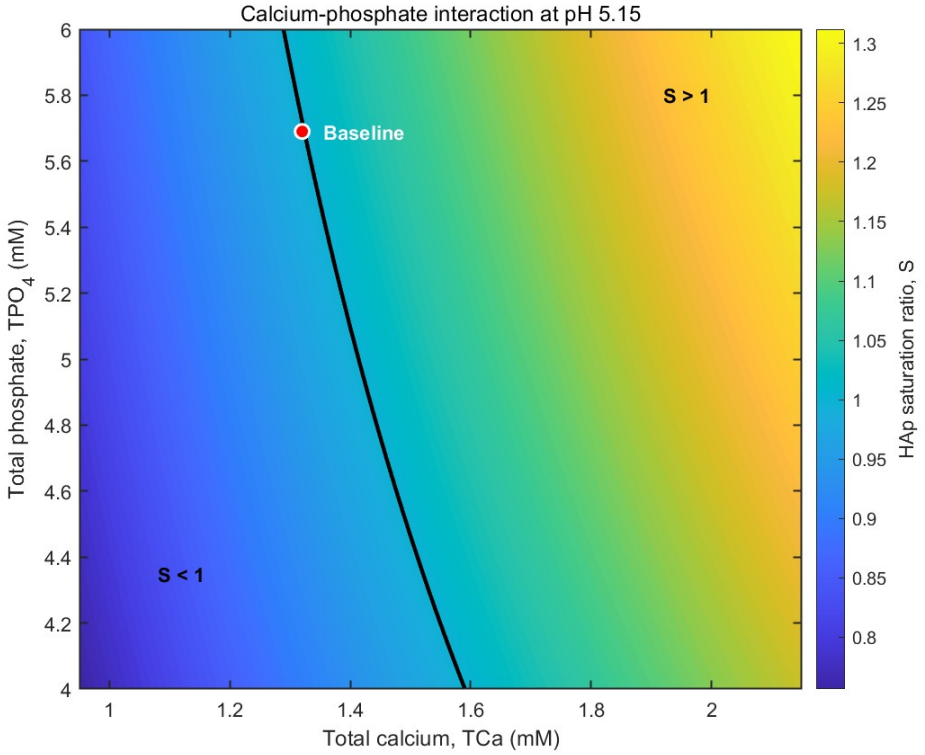


Figure 3.13: Calcium–phosphate interaction map for hydroxyapatite saturation at pH 5.15. The black contour represents $S = 1$, and the red marker indicates the reference saliva composition.

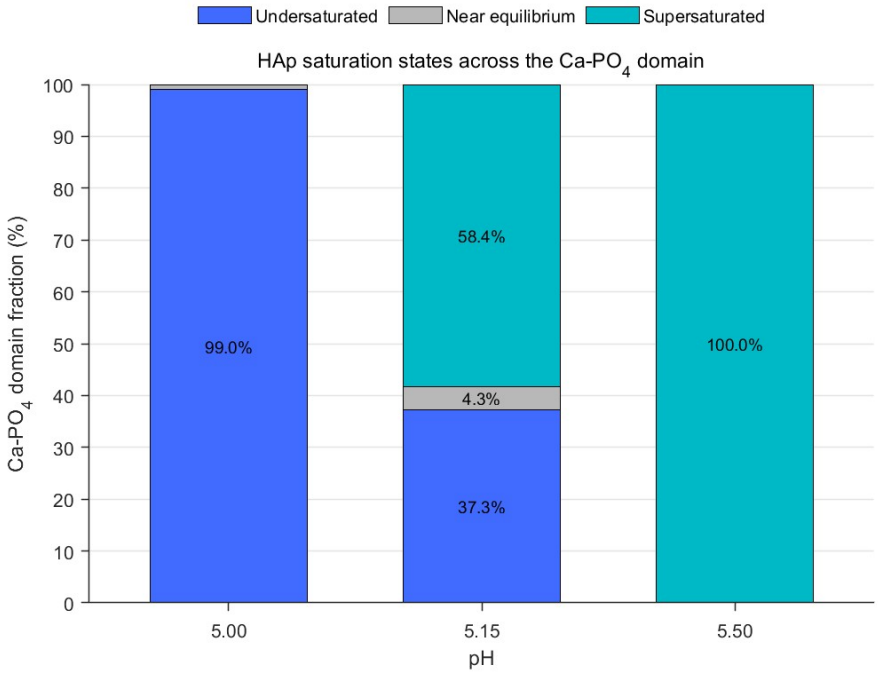


Figure 3.14: Distribution of undersaturated ($S < 0.99$), near-equilibrium ($0.99 \leq S \leq 1.01$), and supersaturated ($S > 1.01$) states across the investigated calcium–phosphate domain at pH 5.00, 5.15, and 5.50.

3.2.5 Multidimensional uncertainty analysis

The exploratory multidimensional uncertainty analysis was performed using 500 independently sampled model compositions within the investigated salivary working ranges, and a valid hydroxyapatite saturation crossover was identified for all simulations. The resulting $pH_{S=1}$ values showed a relatively narrow distribution around the reference condition (Figure 3.15). The mean predicted crossover was 5.1315 with a standard deviation of 0.0753, while the median was 5.1210. Values ranged from 4.9989 to 5.3206. The 2.5th and 97.5th percentiles were 5.0173 and 5.2801, respectively, while the interquartile range extended from 5.0678 to 5.1913 (Table 3.6). The reference saliva crossover of 5.1508 was therefore located close to the center of the simulated distribution.

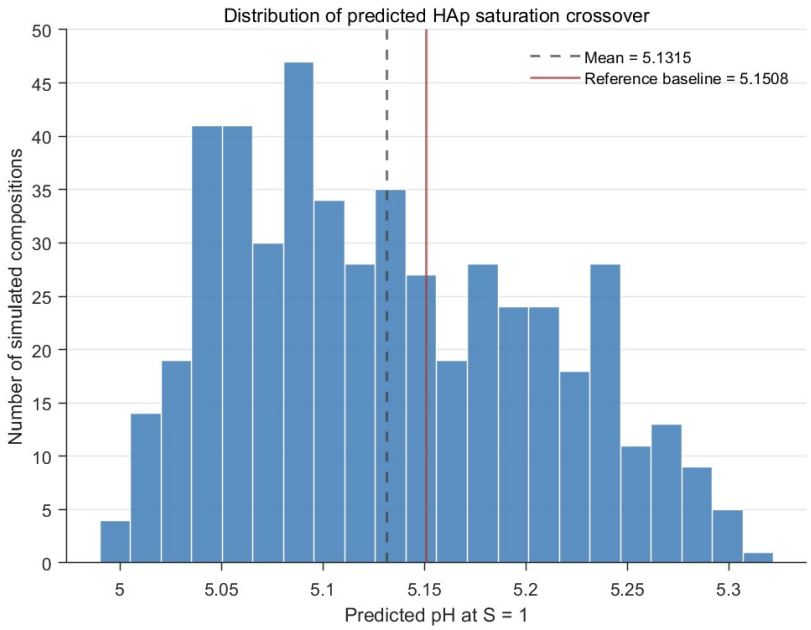


Figure 3.15: Distribution of the predicted hydroxyapatite saturation crossover obtained from 500 randomly sampled model compositions within the investigated salivary working ranges. The dashed line indicates the mean crossover, while the solid reference line indicates the crossover predicted for the reference saliva composition.

Table 3.6: Descriptive statistics of the predicted HAp saturation crossover obtained from the multidimensional uncertainty analysis.

Parameter	**pH at $S = 1$**
Mean	5.1315
Standard deviation	0.0753
Median	5.1210
Minimum	4.9989
Maximum	5.3206
2.5th percentile	5.0173
25th percentile	5.0678
75th percentile	5.1913
97.5th percentile	5.2801

The association between each salivary component and the predicted saturation crossover was further evaluated using Pearson correlation coefficients (Figure 3.16). Calcium showed the strongest association with $pH_{S=1}$, with $r = -0.9608$, followed by phosphate with $r = -0.2235$. The remaining components showed coefficients close to zero: carbonate $r = -0.0126$, magnesium $r = +0.0285$, sodium $r = +0.0045$, potassium $r = +0.0301$, and chloride $r = +0.0070$ (Table 3.7).

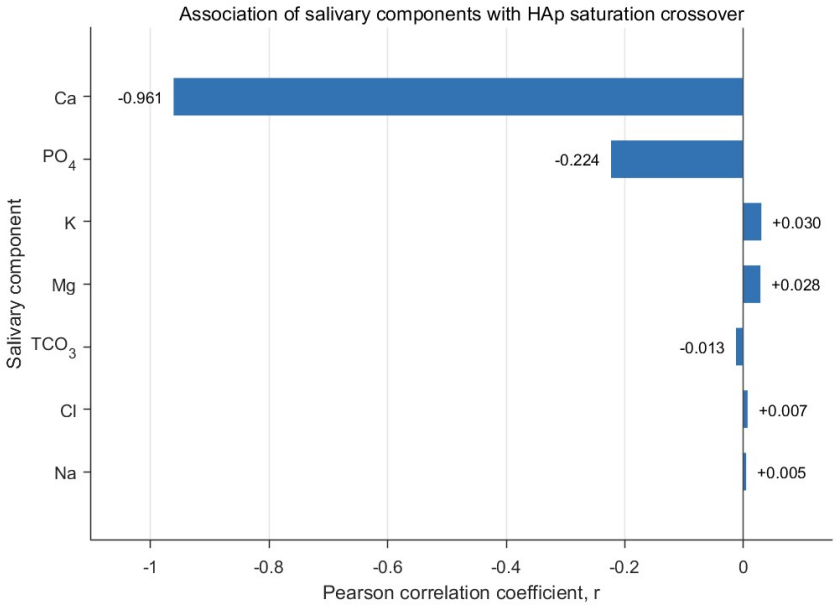


Figure 3.16: Pearson correlation coefficients between the investigated salivary components and the predicted hydroxyapatite saturation crossover.

Table 3.7: Pearson correlation coefficients between salivary ionic components and the predicted HAp saturation crossover.

Salivary component	**Pearson correlation coefficient,** r
Calcium	-0.9608
Phosphate	-0.2235
Carbonate	-0.0126
Magnesium	+0.0285
Sodium	+0.0045
Potassium	+0.0301
Chloride	+0.0070

3.2.6 Thermodynamic characterization of the experimental treatment solutions

The extended equilibrium model was applied to characterize the thermodynamic conditions generated by the experimental remineralization and demineralization solutions. A marked difference in hydroxyapatite saturation was observed between the two treatment environments. The remineralization solution, represented at an input pH of 7.0, was strongly supersaturated with respect to HAp, with a predicted saturation ratio of $S = 18.6133$. In contrast, when the same mineral formulation was evaluated at pH 4.0 in the absence of lactate, the predicted saturation ratio decreased to $S = 0.1465$, corresponding to a markedly undersaturated condition.

Two additional computational reference conditions were used to distinguish the contribution of lactate-containing chemistry from that of acidification alone. When 100 mM lactate was included but Ca–lactate complex formation was disabled ($K_{\mathrm{CaLac}} = 0$), the predicted saturation ratio was $S = 0.1457$, closely matching the pH 4 condition without lactate. When Ca–lactate association was enabled using the representative exploratory value $K_{\mathrm{CaLac}} = 8\,\mathrm{L/mol}$, the saturation ratio decreased further to $S = 0.1354$. Therefore, the largest change in HAp saturation occurred between the pH 7 control and the pH 4 conditions, whereas inclusion of Ca–lactate association produced a smaller additional decrease in saturation.

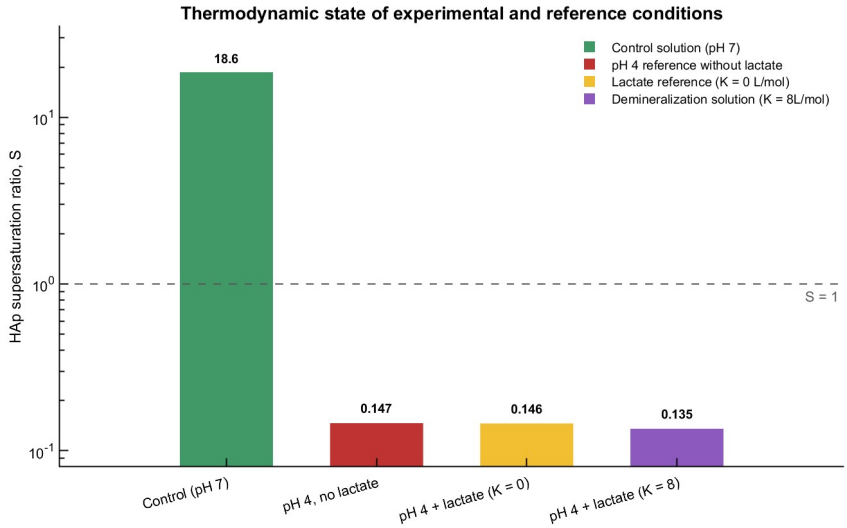


Figure 3.17: Thermodynamic state of the experimental and computational reference conditions. HAp saturation ratios were predicted for the pH 7 control solution, the pH 4 reference condition without lactate, the pH 4 lactate-containing reference condition with Ca–lactate complex formation disabled ($K_{\mathrm{CaLac}} = 0$), and the representative exploratory demineralization condition ($K_{\mathrm{CaLac}} = 8\,\mathrm{L/mol}$). The dashed line indicates the HAp equilibrium condition, $S = 1$.

The principal model-predicted properties of these conditions are summarized in Table 3.8. The lactate-containing simulations required an additional sodium contribution of approximately 66 mM to satisfy electroneutrality. For the representative $K_{\mathrm{CaLac}} = 8\,\mathrm{L/mol}$ condition, the corrected total sodium concentration was 156.066 mM and the final absolute charge-balance residual was 3.05×10^{-9} M. The corresponding ionic strength was 0.3715 M, compared with 0.3076 M in the control solution. Free calcium decreased from 2.2572 mM in the $K_{\mathrm{CaLac}} = 0$ reference condition to 1.9748 mM in the representative $K_{\mathrm{CaLac}} = 8\,\mathrm{L/mol}$ condition, where 12.49% of total calcium was predicted to be present as CaLac^{+}.

Table 3.8: Model-predicted thermodynamic properties of the experimental and computational reference conditions. Additional Na^+ represents the model-derived concentration required to satisfy electroneutrality in the lactate-containing simulations and does not correspond to a directly measured NaOH addition. $K_{CaLac} = 8\,L/mol$ was used as the representative exploratory condition.

Condition	Calculated pH	Ionic strength (M)	Additional Na^+ (mM)	Free Ca^{2+} (mM)	Ca as $CaLac^+$ (%)	HAp S
Remin, pH 7	7.1368	0.3076	–	1.9466	–	18.6133
pH 4, no lactate	4.1366	0.3032	–	2.2534	–	0.1465
pH 4 + lactate, $K_{CaLac} = 0$	4.1382	0.3720	65.907	2.2572	0	0.1457
Demineralization, $K_{CaLac} = 8\,L/mol$	4.1382	0.3715	65.995	1.9748	12.49	0.1354

Sensitivity analysis across the explored Ca–lactate association constants showed a progressive decrease in HAp saturation as the assumed association strength increased. The predicted saturation ratios were 0.1457, 0.1416, 0.1354, and 0.1232 for $K_{CaLac} = 0$, 3, 8, and 20 L/mol, respectively. Despite this variation, all investigated lactate-containing conditions remained below $S = 1$, and the qualitative classification of the solution as undersaturated with respect to HAp was therefore unchanged across the explored range.

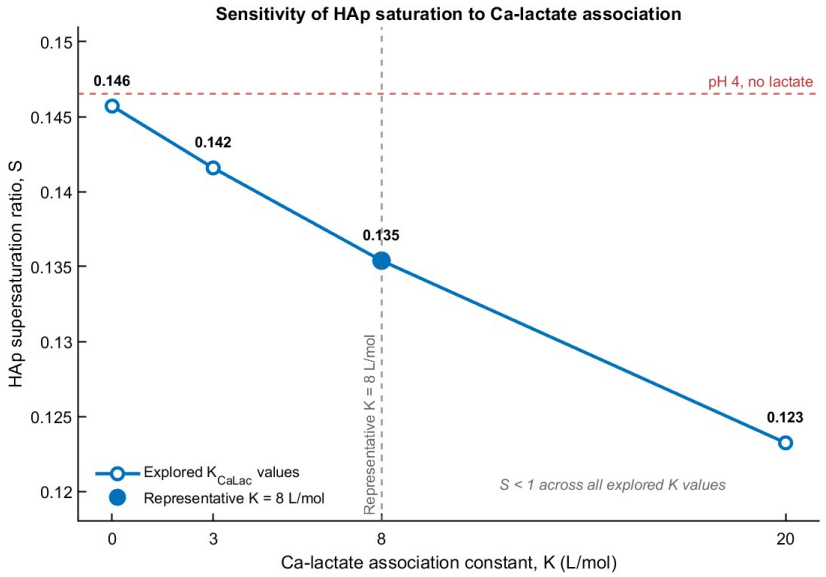


Figure 3.18: Sensitivity of HAp saturation to Ca–lactate association. Predicted HAp saturation ratio as a function of the assumed K_{CaLac}. The horizontal reference indicates the calculated pH 4 condition without lactate, while $K_{CaLac} = 8\,L/mol$ denotes the representative exploratory condition. All explored values remained below $S = 1$.

Changes in HAp saturation were accompanied by a redistribution of calcium among the aqueous species represented in the model. In the $K_{CaLac} = 0$ reference condition, 88.5% of total calcium was present as free Ca^{2+}, while no calcium was present as $CaLac^+$. Increasing K_{CaLac} progressively reduced the fraction of free calcium and increased the fraction associated with $CaLac^+$. At the representative $K_{CaLac} = 8\,L/mol$, approximately 77.4% of total calcium remained as free Ca^{2+}, whereas 12.5% was present as $CaLac^+$. At $K_{CaLac} = 20\,L/mol$, these fractions changed to approximately 65.2% and 26.2%, respectively. The remaining calcium was distributed among the other Ca-containing aqueous species included in the equilibrium model.

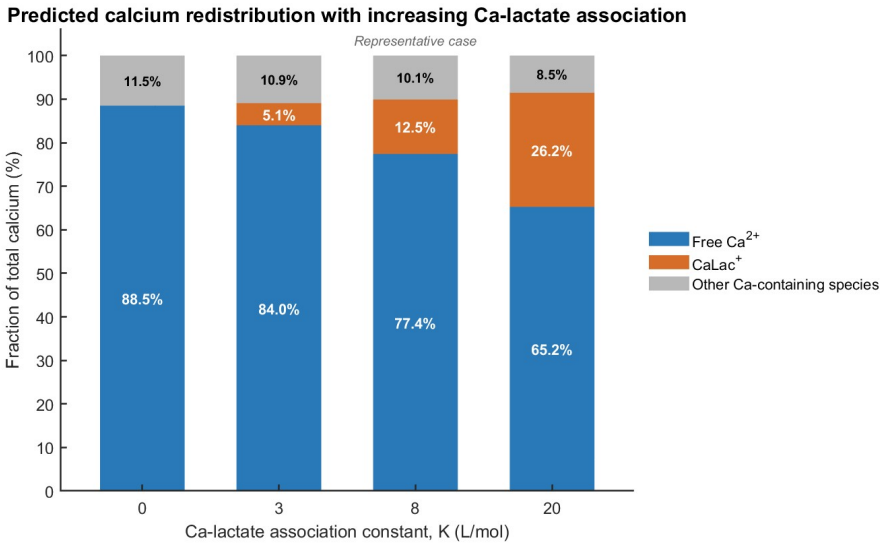


Figure 3.19: Predicted calcium redistribution with increasing Ca–lactate association. Stacked bars represent the fraction of total calcium present as free Ca^{2+}, $CaLac^{+}$, and other Ca-containing aqueous species for each explored K_{CaLac} value. Increasing the assumed Ca–lactate association strength progressively shifted calcium from the free-ion pool toward the $CaLac^{+}$ complex. The $K_{\mathrm{CaLac}} = 8\,\mathrm{L/mol}$ condition was selected as the representative exploratory case.

Chapter 4

Discussion

4.1 Summary of findings

The present study was conducted as an exploratory component of a broader research project aimed at developing controlled experimental models of dental caries. Since the reproduction of caries-like mineral alterations requires the progressive definition of the enamel substrate, treatment conditions, characterization methods, and surrounding physicochemical environment, this work focused on establishing a preliminary workflow rather than reproducing the complete caries process. Two complementary approaches were therefore explored: experimental characterization of bovine enamel and computational investigation of hydroxyapatite (HAp) equilibrium in a saliva-like ionic environment.

The experimental component first established a baseline characterization of untreated bovine enamel. Raman spectroscopy identified the characteristic apatite-related spectral profile, dominated by the phosphate band at approximately 960 cm^{-1}, together with additional phosphate- and carbonate-associated contributions. SEM imaging showed a compact and heterogeneous nanoscale surface organization, while EDS analysis detected prominent calcium, phosphorus, and oxygen signals together with lower-intensity contributions from other elements. Baseline Vickers microhardness measurements provided an additional mechanical characterization, with a mean value of 41.7 ± 2.2 HV0.1.

Following the 6-day experimental treatments, Raman spectroscopy showed that the characteristic apatite fingerprint remained detectable under the Demin, Remin, and Dry conditions. The positions of the main Raman bands remained essentially unchanged, although differences in absolute signal intensity were observed, with the Demin spectra showing a lower intensity of the dominant phosphate band in the direct comparisons. SEM imaging also revealed visually different patterns of surface organization among the three conditions. The Demin specimens exhibited numerous irregular and elongated features arranged locally in compact aggregates, whereas elongated structures were also observed under the Remin condition but appeared more individually distinguishable over the underlying heterogeneous surface. The Dry control showed irregular aggregates with less prominent elongated features. These findings indicate that the investigated treatments were associated with observable differences at the enamel surface; however, their interpretation remains preliminary, particularly because the SEM observations were qualitative and no direct crystallographic identification of the observed structures was performed.

The computational component addressed a different but complementary aspect of the enamel–solution system by investigating the physicochemical conditions governing HAp saturation. The model was adapted from the equilibrium framework previously developed by Poorhemati and Komarova for a biological aqueous environment, in which ionic speciation, ionic strength, activity corrections and HAp supersaturation are simultaneously considered [42]. Following verification of the implementation and adaptation to a saliva-like composition, the model reproduced the expected decrease in HAp saturation upon acidification when compared with experimental salivary ion activity product data [39].

Using the reference saliva composition [38], the model showed that HAp saturation was strongly influenced by pH, with the transition from undersaturation to supersaturation occurring at approximately pH 5.15. This change was also associated with marked variations in phosphate speciation. The sensitivity analysis showed that calcium and phosphate had the greatest influence on the predicted crossover within the investigated ranges, while magnesium, sodium, potassium, chloride, and carbonate had smaller effects.

This general dependence on calcium, phosphate, and pH is consistent with the physicochemical formulation of HAp saturation, which depends on the activities of the mineral-forming ionic species rather than solely on their nominal total concentrations [42, 39].

The literature-based unstimulated and stimulated saliva scenarios further illustrated the effect of variations in the overall salivary environment. The ionic compositions and pH values used to construct these scenarios were derived from reported physiological saliva data [33, 38]. Although the two conditions showed substantially different supersaturation ratios at their respective pH values, their predicted saturation crossover values remained relatively close. Calcium–phosphate interaction maps further demonstrated that, particularly near the saturation boundary, different combinations of calcium and phosphate could shift the system between undersaturated and supersaturated states. The multidimensional uncertainty analysis supported the relative robustness of the predicted crossover within the investigated compositional ranges, while identifying calcium as the component most strongly associated with its variation.

The closest conceptual connection between the computational and experimental components was obtained by applying the extended equilibrium framework to the experimental treatment solutions. The pH 7 Remin/Control environment was predicted to be strongly supersaturated with respect to HAp, whereas the pH 4 demineralization environment was markedly undersaturated. This distinction is consistent with the established physicochemical role of saliva pH and calcium–phosphate availability in determining the tendency toward enamel mineral dissolution or maintenance [7, 39]. Within the exploratory extension of the model, inclusion of Ca–lactate association produced an additional decrease in the predicted HAp saturation through redistribution of calcium from the free-ion pool, although this contribution was substantially smaller than the effect associated with acidification itself.

Importantly, the experimental and computational components were not designed as direct counterparts and should not be interpreted as mutual validation. The experimental analyses describe the characteristics of the enamel substrate and the changes observed following controlled treatments, whereas the computational model describes equilibrium solution chemistry and the thermodynamic tendency toward HAp stability or dissolution. A supersaturated condition therefore indicates that HAp formation or maintenance is thermodynamically permitted within the assumptions of the model, rather than demonstrating

that precipitation or enamel remineralization actually occurred. Conversely, an undersaturated condition provides a thermodynamic environment favourable to mineral dissolution but does not by itself quantify the extent of enamel demineralization.

Overall, the main contribution of this preliminary study is the establishment of an initial experimental–computational framework for investigating enamel mineral behaviour from complementary perspectives. The work defines a baseline characterization strategy, explores the response of bovine enamel to controlled experimental environments, and establishes a saliva-adapted computational approach for investigating HAp saturation and its major physicochemical determinants. Although further development is required before the experimental and computational components can be quantitatively integrated into a model of caries-like lesion formation, the workflow established here provides a foundation for progressively connecting controlled enamel experiments with the physicochemical description of the surrounding solution environment.

4.2 Assumptions and intrinsic limitations

The findings of the present study should be interpreted within the assumptions and intrinsic limitations of both the experimental and computational components. These limitations are particularly relevant because the work was conceived as an exploratory step toward a broader experimental–computational framework for studying caries-like mineral alterations, rather than as a complete model of the caries process.

From an experimental perspective, bovine enamel was used as a model substrate. Although bovine teeth are widely employed as substitutes for human teeth in dental research, differences in composition, microstructure, and physical properties between bovine and human enamel have been reported [12, 17, 16]. The present experimental observations should therefore be regarded as representative of the investigated bovine enamel system and should not be directly extrapolated to human enamel without further validation.

A second limitation concerns the preliminary nature of the experimental characterization. Raman spectroscopy, SEM/EDS, and microhardness provided complementary chemical, morphological, elemental, and mechanical information; however, they were not applied as a fully quantitative multimodal characterization of treatment-induced mineral changes. In particular, the Raman comparisons showed preservation of the characteristic enamel apatite bands together with differences in absolute signal intensity, but these intensity differences alone cannot be interpreted as a direct quantitative measure of mineral loss or gain. Similarly, SEM revealed visually different surface morphologies among the experimental conditions, but no quantitative morphometric analysis was performed. EDS provided elemental information for the baseline enamel characterization, while direct post-treatment quantitative elemental comparisons among the experimental groups were not available. Consequently, the chemical or crystallographic identity of the structures observed by SEM cannot be established from the present measurements alone.

The experimental design also represents a simplified physicochemical environment compared with the oral cavity. The imposed Demin and Remin conditions reproduce selected chemical aspects relevant to mineral dissolution and stability but do not reproduce the complete biological complexity of dental caries. Natural caries development involves dynamic variations in pH, salivary composition and flow, microbial metabolism, diffusion processes,

and repeated demineralization–remineralization episodes [7]. The 6-day treatment conditions used here should therefore be interpreted as controlled experimental environments for exploring enamel response rather than as complete simulations of in vivo caries development.

The computational framework introduces an additional set of assumptions. The model was adapted from the physicochemical equilibrium framework developed by Poorhemati and Komarova [46, 42]. It assumes a homogeneous aqueous environment in which the included chemical species reach equilibrium and uses ionic-strength-dependent activity corrections to estimate the activities of the species contributing to the hydroxyapatite ionic activity product. Consequently, the model describes the thermodynamic state of the solution rather than the kinetics of enamel dissolution, mineral nucleation, crystal growth, or transport at the enamel–solution interface.

Hydroxyapatite was used as the reference mineral phase throughout the computational analysis. This represents a useful approximation for investigating enamel mineral stability but does not reproduce the full complexity of biological enamel apatite, which is non-stoichiometric and contains multiple ionic substitutions [8, 7]. Furthermore, calcium phosphate mineralization can involve precursor or intermediate phases, and precipitation from a supersaturated solution does not necessarily imply the immediate formation of stoichiometric HAp [35, 54]. Accordingly, the calculated supersaturation ratio should be interpreted as a thermodynamic indicator relative to the HAp phase represented in the model, rather than as a direct prediction of the mineral phase formed experimentally.

The saliva-like environment implemented computationally is also necessarily simplified. The model represents the principal inorganic ionic components relevant to HAp equilibrium but does not reproduce the complete composition and structural complexity of human saliva. Natural saliva contains proteins, macromolecules, and other organic and inorganic constituents that can influence ion availability, mineral nucleation, surface interactions, and enamel remineralization [32]. Moreover, salivary composition varies among individuals and between unstimulated and stimulated conditions.[32, 33, 34] The sensitivity, physiological-scenario, and multidimensional analyses performed in this study were intended to explore part of this variability, but they cannot encompass the full biological heterogeneity of the oral environment.

An additional assumption was required when the model was extended to describe the experimental demineralization solution. Since lactate was not included in the original equilibrium framework, Ca–lactate association was added as an exploratory component of the model. The association constant was not assumed to be precisely known for the specific experimental conditions. Instead, a range of values was tested to assess whether changes in the assumed association strength affected the overall thermodynamic classification. Although increasing Ca–lactate association reduced the free-calcium fraction and progressively decreased the predicted HAp saturation ratio, all explored conditions remained markedly undersaturated. The analysis therefore supports the robustness of the qualitative classification within the investigated range, while the quantitative contribution attributed to Ca–lactate complexation should remain exploratory.

Finally, the experimental and computational components were not designed to reproduce identical variables at identical spatial and temporal scales. Raman spectroscopy and

SEM characterize properties of the enamel substrate after treatment, whereas the computational model describes equilibrium properties of the surrounding solution. A direct quantitative correspondence between the predicted HAp saturation ratio and the experimentally observed spectral or morphological changes therefore cannot be established from the present data. The value of combining the two approaches lies instead in their complementarity: the experimental component provides information on the mineral substrate, while the computational component provides a physicochemical description of the environments to which that substrate is exposed. Establishing a direct experimental–computational relationship will require future studies specifically designed to measure solution chemistry and enamel mineral changes under matched conditions and over defined time scales.

4.3 Future experimental and computational developments

A natural next step for this preliminary framework would be to further develop and standardize the experimental protocol for the controlled generation of caries-like lesions in bovine enamel. Increasing the number of specimens and biological replicates, together with the use of well-defined demineralization–remineralization protocols, would allow the reproducibility of the observed changes to be assessed more systematically. Raman spectroscopy, SEM/EDS, and microhardness could then be applied before and after treatment on matched specimens, allowing quantitative changes in mineral composition, surface morphology, elemental composition, and mechanical properties to be directly compared. The inclusion of additional quantitative techniques for assessing mineral loss and lesion depth would further strengthen the characterization of the experimentally generated lesions.

From another perspective, it would be particularly interesting to establish a more direct connection between the experimental and computational components of the framework. Future experiments could be designed using treatment solutions whose ionic composition, pH, and exposure conditions are fully characterized and reproduced as inputs of the computational model. Measurements of the solution composition before and after enamel exposure, together with experimental quantification of enamel mineral changes, would allow the predicted thermodynamic conditions to be compared with the actual response of the mineral substrate. In this way, the computational analysis could progressively move from providing a complementary physicochemical interpretation of the experimental environment toward becoming an integral part of the design and interpretation of controlled demineralization–remineralization experiments.

From a forward-looking perspective, the computational framework could be further extended to more accurately reproduce the dynamic enamel–saliva environment associated with caries development. An ideal model would move beyond a purely equilibrium description by incorporating time-dependent changes in solution chemistry, mineral dissolution and precipitation kinetics, and transport processes occurring at the enamel–solution interface. Additional interactions with relevant salivary components and organic species could also be progressively introduced as experimental information becomes available. Such developments would allow the model to describe not only whether a given solution is thermodynamically favourable or unfavourable to HAp stability, but also how mineral changes

evolve over time. Combined with a standardized experimental model of caries-like lesion formation, this could progressively transform the preliminary workflow developed in the present study into an integrated experimental–computational platform for investigating enamel demineralization and remineralization under increasingly representative conditions.

Chapter 5

Conclusions

This thesis employed an integrated experimental–computational approach to investigate enamel mineral behaviour under controlled physicochemical conditions. The primary objectives were to establish a preliminary experimental workflow for the characterization of bovine enamel and its response to different treatment environments, and to adapt a physicochemical model of hydroxyapatite (HAp) equilibrium to a saliva-like ionic system. Together, these approaches were intended to provide complementary foundations for the broader development of controlled models of caries-like mineral alterations.

The experimental analyses provided an initial characterization of the enamel substrate and of the changes observed following the investigated treatments. Untreated bovine enamel exhibited the characteristic Raman fingerprint of enamel apatite, together with a compact and heterogeneous nanoscale surface morphology and the expected predominance of calcium, phosphorus, and oxygen in the EDS analysis. Baseline microhardness measurements provided additional information on the mechanical properties of the enamel substrate. After the 6-day experimental treatments, the characteristic Raman bands of enamel apatite were still detectable in the Demin, Remin, and Dry conditions, although differences in signal intensity were observed. SEM imaging also showed differences in surface morphology among the three conditions, which became more evident at higher magnification. These results established a preliminary experimental basis for evaluating enamel responses to controlled treatment environments, while also highlighting the need for further quantitative characterization before specific mineral transformations can be established.

Complementing the experimental perspective, a previously developed physicochemical model of HAp equilibrium was adapted to a saliva-like ionic environment. Following verification of the computational implementation, the model demonstrated the strong dependence of HAp saturation on pH and predicted a saturation crossover at approximately pH 5.15 for the reference saliva composition. Sensitivity analyses identified calcium and phosphate as the principal ionic determinants of the predicted crossover within the investigated ranges, while the calcium–phosphate interaction maps demonstrated how their combined variation can determine the transition between undersaturated and supersaturated conditions. The multidimensional analysis further showed that the predicted crossover remained within a relatively narrow range across the investigated variability in salivary

composition, with calcium showing the strongest association with its position.

To establish a first connection between the computational and experimental components, the equilibrium framework was subsequently applied to the solutions used in the experimental treatments. The pH 7 remin/control environment was predicted to be strongly supersaturated with respect to HAp, whereas the pH 4 demineralization environment was markedly undersaturated. The exploratory inclusion of Ca–lactate association produced an additional reduction in HAp saturation by decreasing the free-calcium fraction, although this contribution was smaller than the effect associated with acidification. This analysis provided a thermodynamic characterization of the environments to which the enamel specimens were exposed, without implying a direct quantitative correspondence between the predicted solution saturation state and the experimentally observed enamel changes.

In conclusion, this thesis demonstrates the value of combining experimental characterization of the enamel substrate with physicochemical modelling of the surrounding solution environment. The experimental workflow provides a preliminary platform for investigating enamel responses under controlled conditions, while the saliva-adapted computational model provides a quantitative framework for examining how pH, ionic composition, and chemical speciation influence HAp saturation.

Although the present study does not reproduce the complete complexity of dental caries or establish a direct experimental validation of the computational predictions, it provides an integrated basis for investigating both the enamel substrate and the surrounding solution environment. This integrated approach establishes a foundation for the future development of increasingly controlled and representative experimental–computational models of enamel demineralization and remineralization.

Appendix A

Exploratory quasi-equilibrium response to a plaque-derived pH challenge

.1 Exploratory plaque-derived acidification stress test

An exploratory supplementary analysis was performed to examine how the saliva–hydroxyapatite equilibrium model responds to a transient acidic perturbation representative of the dental plaque microenvironment. The imposed pH trajectory was derived from experimentally observed plaque pH responses following carbohydrate exposure and was therefore not intended to reproduce the temporal evolution of bulk salivary pH [55]. The imposed pH decreased from 7.0 to a minimum of 5.1 at 7 min and subsequently recovered toward baseline, crossing pH 5.5 at approximately 12 min. A 60-min simulation window with a temporal resolution of 0.1 min was used to include both the acidification and recovery phases.

At each time point, the externally prescribed plaque-derived pH value was applied to the reference saliva-like ionic composition, while all total ionic component concentrations were kept constant. The equilibrium calculation was repeated independently at each time point to obtain the corresponding hydroxyapatite supersaturation ratio, $S(t)$. Therefore, this analysis represents a quasi-equilibrium stress test of the reference saliva composition and not a physiological simulation of either plaque fluid or bulk saliva.

For the reference saliva composition, HAp supersaturation decreased to a minimum value of $S = 0.9145$ at 7 min (Figure 1). The system crossed the equilibrium threshold $S = 1$ during acidification at 6.81 min and returned to $S > 1$ at 7.57 min, corresponding to 0.76 min of predicted undersaturation. In comparison, the imposed pH remained below the conventional pH threshold of 5.5 from 5.53 to 12.00 min, corresponding to a total duration of 6.47 min.

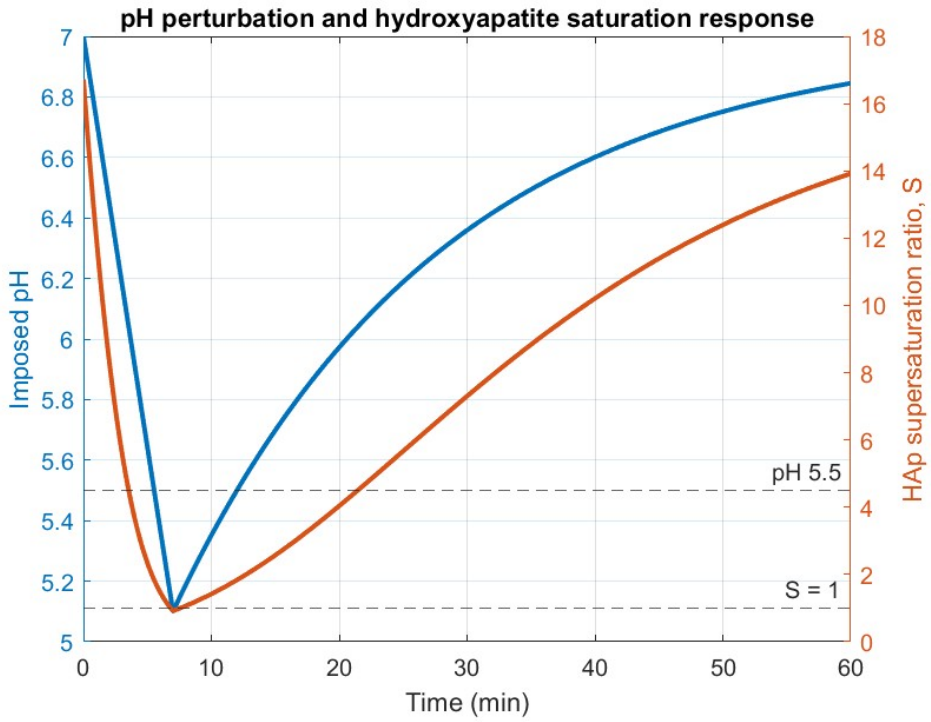


Figure 1: Externally prescribed plaque-derived pH perturbation and corresponding hydroxyapatite saturation response of the reference saliva-like composition. The dashed horizontal lines indicate the conventional pH threshold of 5.5 and the HAp equilibrium condition $S = 1$.

The same imposed pH trajectory was subsequently applied to low, reference, and high calcium conditions of 0.95, 1.32, and 2.15 mM, respectively, while all remaining salivary components were maintained at their reference values. The overall saturation profiles are shown in Figure 2, while Figure 3 provides a magnified view of the region surrounding the acid-challenge minimum and the $S = 1$ threshold.

Reducing total calcium to 0.95 mM resulted in a lower minimum supersaturation ratio of $S = 0.7646$. Under this condition, the system crossed $S = 1$ at 6.44 min during acidification and returned to supersaturation at 8.77 min, corresponding to 2.34 min of undersaturation. Under the reference calcium condition of 1.32 mM, the minimum remained $S = 0.9145$, with 0.76 min spent below $S = 1$. In contrast, increasing total calcium to 2.15 mM maintained the system above the equilibrium threshold throughout the entire imposed perturbation. The minimum supersaturation ratio in this condition was $S = 1.1892$, and no $S = 1$ crossing occurred.

Table 1: Calcium-dependent hydroxyapatite saturation response during the exploratory plaque-derived acidification stress test.

Calcium condition	Minimum S	Time of minimum (min)	Downward $S = 1$ crossing (min)	Recovery $S = 1$ crossing (min)	Time with $S < 1$ (min)
Low Ca (0.95 mM)	0.7646	7.00	6.44	8.77	2.34
Reference Ca (1.32 mM)	0.9145	7.00	6.81	7.57	0.76
High Ca (2.15 mM)	1.1892	7.00	–	–	0.00

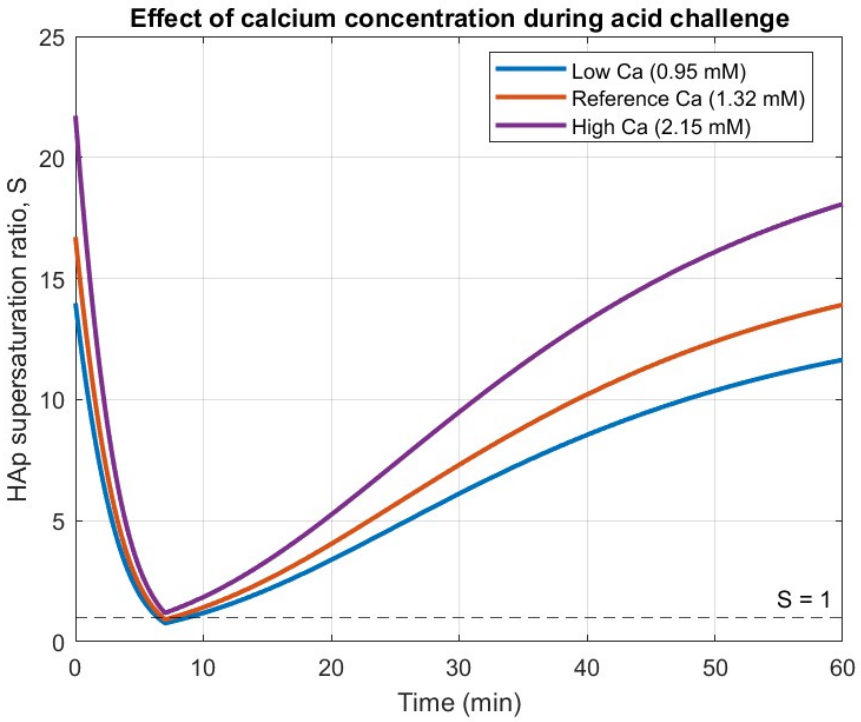


Figure 2: Hydroxyapatite supersaturation ratio over the complete 60-min acidification stress test under low, reference, and high total calcium conditions. The dashed horizontal line indicates the equilibrium threshold $S = 1$.

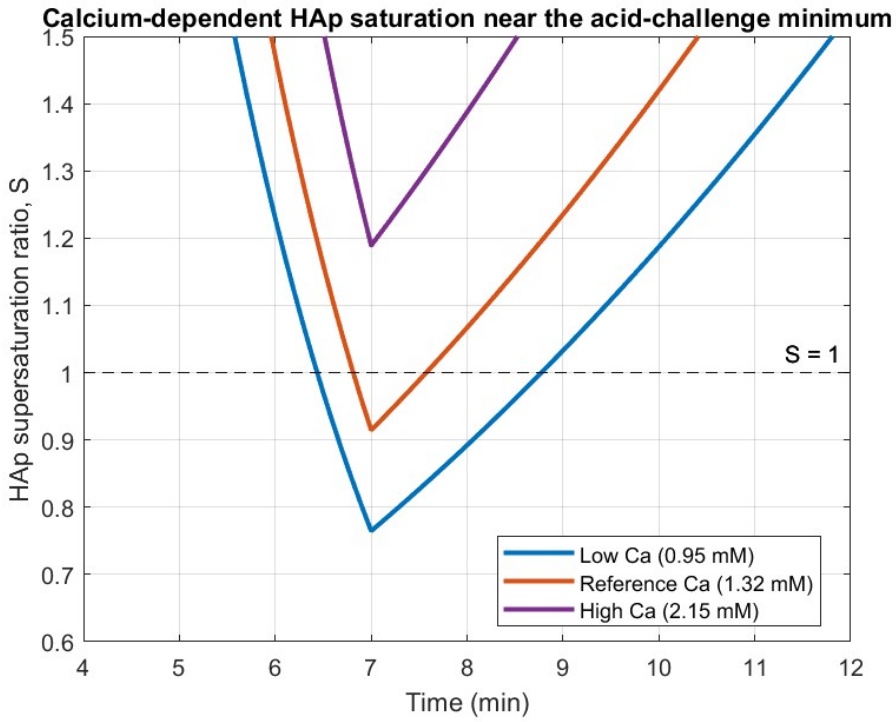


Figure 3: Magnified view of the calcium-dependent HAp saturation response around the minimum of the imposed acid challenge. The dashed horizontal line indicates the equilibrium condition $S = 1$.

Overall, lower calcium availability increased both the magnitude and duration of the excursion below $S = 1$, whereas the high-calcium condition remained supersaturated throughout the imposed pH perturbation. This behaviour is consistent with the strong calcium dependence identified in the sensitivity analyses presented in the main text.

These results should not be interpreted as a physiological simulation of either salivary or plaque chemistry. The pH trajectory was derived from plaque measurements, whereas the ionic composition corresponded to the reference saliva model. In addition, no time-dependent changes in ionic composition, transport processes, buffering kinetics, mineral mass balance, or dissolution/precipitation kinetics were represented. The analysis was therefore retained only as an exploratory stress test of the equilibrium framework.

References

[1] Andrew H. Jheon et al. “From molecules to mastication: the development and evolution of teeth”. In: *Wiley Interdisciplinary Reviews: Developmental Biology* 2.2 (2013), pp. 165–183. DOI: 10.1002/wdev.63.

[2] Elizabeth A. Ronan, Maximilian Nagel, and Joshua J. Emrick. “The anatomy, neurophysiology, and cellular mechanisms of intradental sensation”. In: *Frontiers in Pain Research* 5 (2024), p. 1376564. DOI: 10.3389/fpain.2024.1376564.

[3] Rodrigo S. Lacruz et al. “Dental Enamel Formation and Implications for Oral Health and Disease”. In: *Physiological Reviews* 97 (2017), pp. 939–993. DOI: 10.1152/physrev.00030.2016.

[4] Ezgi D. Yilmaz, Gerold A. Schneider, and Michael V. Swain. “Influence of structural hierarchy on the fracture behaviour of tooth enamel”. In: *Philosophical Transactions of the Royal Society A: Mathematical, Physical and Engineering Sciences* 373 (2015), p. 20140130. DOI: 10.1098/rsta.2014.0130.

[5] Jayasudha et al. “Enamel Regeneration—Current Progress and Challenges”. In: *Journal of Clinical and Diagnostic Research* 8.9 (2014), ZE06–ZE09. DOI: 10.7860/JCDR/2014/10231.4883.

[6] Rodrigo S. Lacruz. “Enamel: Molecular identity of its transepithelial ion transport system”. In: *Cell Calcium* 65 (2017), pp. 1–7. DOI: 10.1016/j.ceca.2017.03.006.

[7] Ensanya Ali Abou Neel et al. “Demineralization–remineralization dynamics in teeth and bone”. In: *International Journal of Nanomedicine* 11 (2016), pp. 4743–4763. DOI: 10.2147/IJN.S107624.

[8] E. D. Eanes. “Enamel Apatite: Chemistry, Structure and Properties”. In: *Journal of Dental Research* 58.2 Suppl (1979), pp. 829–834. DOI: 10.1177/00220345790580023501.

[9] Katarzyna Sarna-Bos et al. “Elemental mapping of human teeth enamel, dentine and cementum in view of their microstructure”. In: *Micron* 172 (2023), p. 103485. DOI: 10.1016/j.micron.2023.103485.

[10] R. Z. LeGeros et al. “Magnesium and carbonate in enamel and synthetic apatites”. In: *Advances in Dental Research* 10.2 (1996), pp. 225–231. DOI: 10.1177/08959374960100021801.

[11] Eisha Imran et al. “Dental Applications of Ion-Substituted Hydroxyapatite: A Review of the Literature”. In: *Dentistry Journal* 12 (2024), p. 304. DOI: 10.3390/dj12100304.

[12] Ghaeth H. Yassen, Jeffrey A. Platt, and Anderson T. Hara. "Bovine teeth as substitute for human teeth in dental research: a review of literature". In: *Journal of Oral Science* 53.3 (2011), pp. 273–282.

[13] Yipeng Fu et al. "In Vitro Models Used in Cariology Mineralisation Research—A Review of the Literature". In: *Dentistry Journal* 12 (2024), p. 323. DOI: 10.3390/dj12100323.

[14] Mahmoud Al Ankily et al. "Bovine Teeth as Substitutes for Human Teeth in Dental Research: Ultrastructural and Radiographic Analysis". In: *European Journal of Dentistry* 20.2 (2026), pp. 457–465. DOI: 10.1055/s-0045-1809032.

[15] P. Laurance-Young et al. "A review of the structure of human and bovine dental hard tissues and their physicochemical behaviour in relation to erosive challenge and remineralisation". In: *Journal of Dentistry* 39.4 (2011), pp. 266–272. DOI: 10.1016/j.jdent.2011.01.008.

[16] Chaoyang Wang et al. "Enamel microstructural features of bovine and human incisors: A comparative study". In: *Annals of Anatomy* 235 (2021), p. 151700. DOI: 10.1016/j.aanat.2021.151700.

[17] Juan de Dios Teruel et al. "Comparison of chemical composition of enamel and dentine in human, bovine, porcine and ovine teeth". In: *Archives of Oral Biology* 60.5 (2015), pp. 768–775. DOI: 10.1016/j.archoralbio.2015.01.014.

[18] Santiago Arango-Santander et al. "Chemical, structural and mechanical characterization of bovine enamel". In: *Archives of Oral Biology* 109 (2020), p. 104573. DOI: 10.1016/j.archoralbio.2019.104573.

[19] Frank Lippert and Robert J. M. Lynch. "Comparison of Knoop and Vickers surface microhardness and transverse microradiography for the study of early caries lesion formation in human and bovine enamel". In: *Archives of Oral Biology* 59.7 (2014), pp. 704–710. DOI: 10.1016/j.archoralbio.2014.04.005.

[20] Marwa Abdelaziz. "Detection, Diagnosis, and Monitoring of Early Caries: The Future of Individualized Dental Care". In: *Diagnostics* 13 (2023), p. 3649. DOI: 10.3390/diagnostics13243649.

[21] Giuseppina Malcangi et al. "Analysis of Dental Enamel Remineralization: A Systematic Review of Technique Comparisons". In: *Bioengineering* 10 (2023), p. 472. DOI: 10.3390/bioengineering10040472.

[22] Peiyan Shen et al. "Efficient enamel subsurface lesion remineralisation and dentine tubule occlusion by high concentration CPP-ACP: a randomised, cross-over in situ study". In: *Scientific Reports* 15 (2025), p. 28263. DOI: 10.1038/s41598-025-14005-z.

[23] John D. B. Featherstone. "Caries prevention and reversal based on the caries balance". In: *Pediatric Dentistry* 28.2 (2006), pp. 128–132.

[24] S. Lata, N. O. Varghese, and Jolly Mary Varughese. "Remineralization potential of fluoride and amorphous calcium phosphate-casein phospho peptide on enamel lesions: An in vitro comparative evaluation". In: *Journal of Conservative Dentistry* 13.1 (2010), pp. 42–46. DOI: 10.4103/0972-0707.62634.

[25] Namrata Patil et al. “Comparative evaluation of remineralizing potential of three agents on artificially demineralized human enamel: An in vitro study”. In: *Journal of Conservative Dentistry* 16.2 (2013), pp. 116–120. DOI: 10.4103/0972-0707.108185.

[26] Siti N. B. Mohd Said, Manikandan Ekambaram, and Cynthia K. Y. Yiu. “Effect of different fluoride varnishes on remineralization of artificial enamel carious lesions”. In: *International Journal of Paediatric Dentistry* 27.3 (2017), pp. 163–173. DOI: 10.1111/ipd.12243.

[27] Sai Sathya Narayana et al. “Remineralization efficiency of bioactive glass on artificially induced carious lesion an in-vitro study”. In: *Journal of Indian Society of Pedodontics and Preventive Dentistry* 32.1 (2014), pp. 19–25. DOI: 10.4103/0970-4388.127047.

[28] Fahimeh Farzanegan et al. “An In Vitro Study on the Effect of Amorphous Calcium Phosphate and Fluoride Solutions on Color Improvement of White Spot Lesions”. In: *Dentistry Journal* 6.3 (2018), p. 24. DOI: 10.3390/dj6030024.

[29] Chintan Joshi et al. “Comparative Evaluation of the Remineralizing Potential of Commercially Available Agents on Artificially Demineralized Human Enamel: An In Vitro Study”. In: *Contemporary Clinical Dentistry* 10.4 (2019), pp. 605–613. DOI: 10.4103/ccd.ccd_679_18.

[30] Raisa Queiroz Catunda et al. “Pre-treatment oral microbiome analysis and salivary Stephan curve kinetics in white spot lesion development in orthodontic patients wearing fixed appliances: a pilot study”. In: *BMC Oral Health* 23 (2023), p. 239. DOI: 10.1186/s12903-023-02917-z.

[31] Colin Dawes. “What Is the Critical pH and Why Does a Tooth Dissolve in Acid?” In: *Journal of the Canadian Dental Association* 69.11 (2003), pp. 722–724.

[32] Anwesha Sarkar, Feng Xu, and Seunghwan Lee. “Human saliva and model saliva at bulk to adsorbed phases—similarities and differences”. In: *Advances in Colloid and Interface Science* 273 (2019), p. 102034. DOI: 10.1016/j.cis.2019.102034.

[33] Gerald Schwerdt et al. “Physiological regulation of oral saliva ion composition and flow rate are not coupled in healthy humans—Partial revision of our current knowledge required”. In: *Pflügers Archiv - European Journal of Physiology* 477 (2025), pp. 55–65. DOI: 10.1007/s00424-024-03025-9.

[34] M. J. Larsen et al. “Individual variations of pH, buffer capacity, and concentrations of calcium and phosphate in unstimulated whole saliva”. In: *Archives of Oral Biology* 44.2 (1999), pp. 111–117. DOI: 10.1016/S0003-9969(98)00108-3.

[35] Y. Sato et al. “Precipitation of octacalcium phosphates on artificial enamel in artificial saliva”. In: *Journal of Materials Science: Materials in Medicine* 17 (2006), pp. 1173–1177. DOI: 10.1007/s10856-006-0545-4.

[36] Marcin Urbanowicz et al. “Simultaneous Determination of Na^+, K^+, Ca^{2+}, Mg^{2+} and Cl^- in Unstimulated and Stimulated Human Saliva Using All Solid State Multisensor Platform”. In: *Electroanalysis* 29 (2017). DOI: 10.1002/elan.201700149.

[37] Colin Dawes. “Salivary flow patterns and the health of hard and soft oral tissues”. In: *The Journal of the American Dental Association* 139.Supplement 2 (2008), 18S–24S. DOI: 10.14219/jada.archive.2008.0351.

[38] Hitoshi Uchida and Catherine E. Ovitt. "Novel impacts of saliva with regard to oral health". In: *The Journal of Prosthetic Dentistry* 127.3 (2022), pp. 383–391. DOI: 10.1016/j.prosdent.2021.05.009.

[39] H. Aiuchi et al. "Relationship between quantitative assessments of salivary buffering capacity and ion activity product for hydroxyapatite in relation to cariogenic potential". In: *Australian Dental Journal* 53.2 (2008), pp. 167–171. DOI: 10.1111/j.1834-7819.2008.00027.x.

[40] C. M. Carey and G. L. Vogel. "Measurement of Calcium Activity in Oral Fluids by Ion Selective Electrode: Method Evaluation and Simplified Calculation of Ion Activity Products". In: *Journal of Research of the National Institute of Standards and Technology* 105.2 (2000), pp. 267–273.

[41] M. J. Larsen and E. I. F. Pearce. "Saturation of human saliva with respect to calcium salts". In: *Archives of Oral Biology* 48.4 (2003), pp. 317–322. DOI: 10.1016/S0003-9969(03)00007-4.

[42] Hossein Poorhemati and Svetlana V. Komarova. "Mathematical model of physicochemical regulation of precipitation of bone hydroxyapatite". In: *Frontiers in Applied Mathematics and Statistics* 9 (2023), p. 1294540. DOI: 10.3389/fams.2023.1294540.

[43] Otakar Söhnel and Felix Grases. "Supersaturation of body fluids, plasma and urine, with respect to biological hydroxyapatite". In: *Urological Research* 39 (2011), pp. 429–436. DOI: 10.1007/s00240-011-0387-5.

[44] M. J. Larsen. "Degrees of saturation with respect to apatites in parotid saliva at various pH values". In: *Scandinavian Journal of Dental Research* 83.1 (1975), pp. 7–12. DOI: 10.1111/j.1600-0722.1975.tb00412.x.

[45] H.-B. Pan and B. W. Darvell. "Solubility of hydroxyapatite by solid titration at pH 3–4". In: *Archives of Oral Biology* 52.7 (2007), pp. 618–624. DOI: 10.1016/j.archoralbio.2006.12.007.

[46] Hossein Poorhemati and Svetlana V. Komarova. "Mathematical modeling of the role of bone turnover in pH regulation in bone interstitial fluid". In: *Computational Biology and Chemistry* 94 (2021), p. 107564. DOI: 10.1016/j.compbiolchem.2021.107564.

[47] Alex C.-T. Ko et al. "Ex vivo detection and characterization of early dental caries by optical coherence tomography and Raman spectroscopy". In: *Journal of Biomedical Optics* 10.3 (2005), p. 031118. DOI: 10.1117/1.1915488.

[48] Abdulmajeed Mohammed Alhussain et al. "Remineralization of artificial carious lesions using a novel fluoride incorporated bioactive glass dentifrice". In: *Dental and Medical Problems* 55.4 (2018), pp. 379–382. DOI: 10.17219/dmp/97311.

[49] Rand Al-Obaidi et al. "Formation and assessment of enamel subsurface lesions in vitro". In: *Journal of Oral Science* 61.3 (2019), pp. 454–458. DOI: 10.2334/josnusd.18-0174.

[50] B. Mohanty et al. "Characterizing and identifying incipient carious lesions in dental enamel using micro-Raman spectroscopy". In: *Caries Research* 47.1 (2013), pp. 27–33. DOI: 10.1159/000342432.

[51] Hossein Poorhemati and Svetlana V. Komarova. "Mathematical model capturing physicochemical and biological regulation of bone mineralization". In: *Scientific Reports* 14 (2024), p. 29831. DOI: 10.1038/s41598-024-81472-1.

[52] R. Portanova et al. "Critical evaluation of stability constants for alpha-hydroxycarboxylic acid complexes with protons and metal ions and the accompanying enthalpy changes. Part II. Aliphatic 2-hydroxycarboxylic acids". In: *Pure and Applied Chemistry* 75.4 (2003), pp. 495–540. DOI: 10.1351/pac200375040495.

[53] Martina Vavrusova, Merete Bøgelund Munk, and Leif H. Skibsted. "Aqueous Solubility of Calcium L-Lactate, Calcium D-Gluconate, and Calcium D-Lactobionate: Importance of Complex Formation for Solubility Increase by Hydroxycarboxylate Mixtures". In: *Journal of Agricultural and Food Chemistry* 61.34 (2013), pp. 8207–8214. DOI: 10.1021/jf402124n.

[54] Joachim Enax et al. "The Remineralization of Enamel from Saliva: A Chemical Perspective". In: *Dentistry Journal* 12.11 (2024), p. 339. DOI: 10.3390/dj12110339.

[55] Sunil Mankar et al. "Clinical Evaluation of the Effect of Nanohydroxyapatite Lozenge on the pH of Dental Plaque". In: *Clinical, Cosmetic and Investigational Dentistry* 16 (2024), pp. 285–293. DOI: 10.2147/CCIDE.S472427.